ELSEVIER

Contents lists available at ScienceDirect

Powder Technology

journal homepage: www.journals.elsevier.com/powder-technology





A moving porous media model for continuous spatial particle ALD

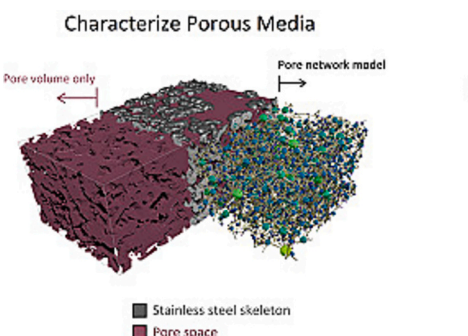
Julia Hartig ^a, Vidumin Dahanayake ^b, Julie Nguyen ^a, Carter Wilson ^a, Austin M. Barnes ^c, Alan W. Weimer ^a, *

- ^a Department of Chemical and Biological Engineering, University of Colorado Boulder, Boulder, CO 80309, USA
- ^b Anton Paar USA, Inc., Ashland, VA 23005, USA
- ^c Covalent Metrology Services Inc., Sunnyvale, CA 94085, USA

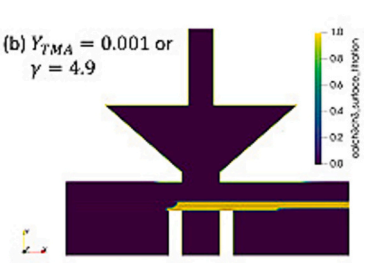
HIGHLIGHTS

- A moving porous media model was developed for continuous spatial particle ALD.
- Powder bed convection was simulated using the dynamic mesh method.
- Optimal inlet precursor mass fraction was quantified using excess number.
- CVD reactions were observed in the first precursor zone.

GRAPHICAL ABSTRACT



Simulate Reactor Conditions



ARTICLE INFO

Keywords:
Porous media
Darcy's law
Atomic layer deposition
CFD
Dynamic mesh

ABSTRACT

A moving porous media (MPM) modeling methodology was developed for reactor-scale CFD simulations of continuous spatial particle atomic layer deposition (ALD). The continuous vibrating reactor process for particle atomic layer deposition (CVR-ALD) was modeled by treating the powder bed as a porous media which conveys as a sliding and layering dynamic mesh zone inside the vibrating reactor zone. Candidate porous reactor baseplates were experimentally characterized using x-ray computed tomography (XRCT), porometry, porosimetry, and atomic force microscopy (AFM) before permeabilities from flow tests were used as inputs to the MPM model. Parameter sweeps over vibration magnitude, powder bed convection speed, and precursor mass fraction revealed the dependence of surface titration uniformity and residual gas breakthrough on operating conditions and powder properties. Parasitic chemical vapor deposition (CVD) reactions were observed in the first precursor zone when dose start times and inlet gas compositions were not optimized.

1. Introduction

Atomic layer deposition (ALD) is a coating technique used to produce

thin films with atomic-level thickness control. In ALD, self-limited reactions between the substrate surface and gaseous precursors enable the synthesis of highly conformal and precise nanofilms. Simulations and

https://doi.org/10.1016/j.powtec.2023.118448

^{*} Corresponding author.

E-mail address: alan.weimer@colorado.edu (A.W. Weimer).

modeling from the atomic level to the continuum scale have contributed to our multiscale understanding of the behavior inside ALD reactors. Investigations into the atomic and mesoscales include density functional theory (DFT) simulations, molecular dynamics simulations [1], growth mode deposition models [2], and ballistic transport models [3]. Monte Carlo methods discretize the surface to be coated and use probabilistic trajectories to identify reaction sites and track surface coverage [4,5]. Continuum models for deposition provide clarity on the reactive transport of species to and from the substrate surface. These vary in complexity from solving the diffusion equation with surface reactions [6,7] to highly coupled computational fluid dynamics (CFD) solvers for the reactor cavity [8-15]. Reaction kinetic expressions may be derived from Langmuir's equation [7,16], kinetic theory [17] or kinetic Monte Carlo models [10,18]. Physics-based analytical expressions have also been developed to describe spatial atomic layer deposition on moving substrates [19,20].

Particle ALD refers to an ALD film on a particle substrate and uses different reactor configurations than the systems from existing CFD modeling studies on planar substrates. ALD films can be deposited onto batches of particles using fixed-bed [21], fluidized-bed [22], or rotarydrum [23,24] reactors. In high-throughput manufacturing environments, continuous particle processing methods have also been employed [25-27]. A continuous vibrating reactor for spatial particle atomic layer deposition (CVR-ALD) [28] was recently developed for large-scale particle ALD. Also referred to as continuous spatial particle ALD reactors, CVR-ALD reactors use linear vibration to continuously transport particles through alternating regions of inert purge gas and dilute precursor in a carrier gas. Purge zones are needed to prevent precursor gases from coming into contact and forming solid nanoparticles through chemical vapor deposition (CVD) reactions, which may deposit on the substrate to produce porous, non-self-limited films. Vibration is known to promote gas-solid contact and film uniformity in batch particle ALD systems [29] but its effect on the gas-phase diffusion of dilute ALD precursors through an inert carrier gas has not yet been quantified. Non-self-limited CVD reactions between precursor gases become more difficult to avoid during concurrent dosing and will depend on diffusion extent of the ALD precursor front.

Capital cost and desired operating conditions also influence the CVR-ALD system design for specific film and substrate chemistry combinations. The minimum purge zone size required to keep CVD byproducts below experimental targets will be process dependent. High precursor utilization can be achieved in particle ALD [22,30] but is challenging to monitor downstream in CVR-ALD where precursor and product gases are diluted by purge gas. Surface titration uniformity, which refers to the sterically hindered film or ligand coverage after one ALD cycle and may be less than one monolayer [2,31,32], requires saturating doses of often expensive precursor gases [8,30]. How to maximize surface titration uniformity while minimizing precursor utilization and other questions about reactive transport behavior can be investigated in a continuum-scale CFD model for CVR-ALD.

Continuum approaches to the gas phase have been well-documented and well-validated for many gases in the literature [33]. Continuum treatments of the solids phase and gas-solid interactions, on the other hand, are more restrictive and require justification [34,35]. Packed-bed-like solids flow behavior was observed in the CVR-ALD reactor at low vibration intensities in our previous work [26] and enables the powder bed to be treated as a porous media [36–38] characterized by viscous and inertial resistances [39]. Viscous resistance, or inverse permeability from Darcy's law, depends on the powder bed's porosity, packing orientation, and particle shape [40]. A reacting moving porous media (MPM) model can explore how powder bed properties such as specific surface area and site density lead to changes in the residual gas concentration and bed surface titration uniformity.

The permeability of a porous medium depends on geometric properties of the fluid channels forming flow paths in the solid skeleton. Many permeability correlations contain empirical fitting factors relating

to pore network parameters that are difficult to measure experimentally. The original Carman-Kozeny or Kozeny-Carman equation [41,42] is often referred to as the most basic permeability equation and calculates permeability α from the void fraction ε and the pore surface area per unit total volume s_{tv} as

$$\alpha = \frac{1}{c_0} \frac{\varepsilon^3}{s_{c_0}^2} \tag{1}$$

where c_0 is the Kozeny or Kozeny-Carman (KC) constant and generally assigned a value of five [43]. Specific surface area in the Kozeny-Carman equation can also be written in terms of the solid volume, $s_{sv} = s_{tv}/(1-\varepsilon)$, as [43]

$$\alpha = \frac{1}{c_0} \frac{\varepsilon^3}{\left(1 - \varepsilon\right)^2 s_{vv}^2} \tag{2}$$

For an unconsolidated bed of spheres, the specific surface area can be replaced with $s_{sv}=6/d_{eff}$ where d_{eff} is the effective particle diameter [44]. The Kozeny-Carman equation for spherical packings is commonly written with the d_{eff} substitution for specific surface area [45] as

$$\alpha = \frac{d_{eff}^2}{36} \frac{\varepsilon^3}{c_0 (1 - \varepsilon)^2} \tag{3}$$

The Kozeny constant corrects for differences in pore connectivity between materials with the same solid specific surface area and porosity. Some studies have used the expression $c\tau^2$ for c_0 where c is a pore shape factor (equivalent to b/16 from the capillary form of the Eqs. [46]) and τ is the tortuosity, a ratio between the effective pore path length and the shortest distance from pore inlet to outlet (i.e. the material thickness L) [47]: L_e/L . The $c_0=5$ value mentioned previously comes from assuming a shape factor c=2.5 and a tortuosity $\tau=\sqrt{2}$ [48]. Referring to c_0 as a Kozeny "constant" can be misleading for materials with pore shape factors and tortuosities that change with time. The ALD-coated porous media in this study have film thicknesses on the order of 1–10 nm (\leq 50 ALD cycles with \sim 0.12 nm/cycle of alumina) [31], many orders of magnitude smaller than the mean pore diameters (\sim 10–20 µm), so ALD film thickness is not expected to have a significant effect on the Kozeny constant.

Tortuosity values range from one for the shortest path from point A to point B (i.e., a line) to high numbers for long, circuitous pore paths. Tortuosity can be calculated using empirical models or diffusion experiments [49], simulations based on image data [50], or porosimetry correlations [51]. The definition of the dimensionless parameter tortuosity varies between publications and has been discussed in several reviews [46,52]. Studies can be found defining tortuosity as a path length ratio [41,53], L_e/L , or as a "tortuosity factor" [54–56] using the square of this path length ratio, $(L_e/L)^2$. Throughout this paper, tortuosity will refer to the ratio of the path lengths, not the tortuosity factor: $\tau \equiv (L_e/L)$.

In this work, we propose a reacting MPM model in ANSYS Fluent to capture the reacting multiphase flow behavior inside CVR-ALD reactors. The powder bed is approximated as a porous media which conveys as a sliding and layering dynamic mesh zone inside the vibrating (2D rigid body translation) reactor dynamic mesh zone. The porous baseplate or "frit" is also included as a porous media zone which moves with the reactor. Heterogeneous half-reactions (ALD) and homogeneous volume reactions (CVD) are modeled using first-order Arrhenius kinetics. Inputs to the MPM model such as frit and packed bed permeability, porosity, and velocity are derived from pressure drop versus gas velocity curves and previously acquired DEM data [57].

2. Methods

2.1. Materials

The CVR-ALD reactor has two key components which change in composition depending on the application: the powder substrate and the

porous frit. In this study, soda lime glass beads (45–63 µm in diameter, from Mo-Sci Corporation) were chosen as an ideal, mildly cohesive Geldart A powder substrate. Powders of this size fluidize intermittently during vibratory convection, exhibiting clear distinctions between liftoff and contact that can be applied as a piecewise velocity profile in the porous media dynamic meshing model [57]. Three inert frit materials with sieve diameters ~10 µm were also selected: a sintered stainlesssteel powder sheet (Mott Corporation, part number 1100-10-40-0.062-10-A SHEET 316LSS), a sintered stainless-steel felt, and a sintered stainless-steel mesh (TWP-Inc, part number MIC10TL5). The 5-ply mesh material consists of two coarse layers (12 \times 64 mesh size), two fine layers (100 mesh) and one ultrafine layer (165 \times 1400 mesh). These frits represent porous materials with varying pore geometry suitable for a particle ALD reactor. The sintered mesh and sintered powder materials are approximately 1.6-mm thick and can be placed directly in the reactor frit cavity. The felt material is only 0.5-mm thick so several felt layers were stacked to match the sintered mesh and sintered powder material thicknesses.

2.2. Porous media analysis

To better understand how the porous baseplate geometry affects gas transport behavior, each of the three candidate frit materials was characterized by tomography, porometry, and porosimetry. X-ray computed tomography (XRCT) images of the porous baseplate samples were obtained using a Zeiss Xradia 520 Versa CT microscope at the University of Colorado's Materials Instrumentation and Multimodal Imaging Core Facility (MIMIC, RRID:SCR 019307). Square samples 2- to 6-mm in length were scanned using a 140 kV source voltage with the settings shown in Table 1. Voxel resolutions were chosen to maximize the field of view while resolving the minimum characteristic feature size $(1.05 \ \mu m, \, 1.05 \ \mu m, \, and \, 5.97 \ \mu m$ for the sintered powder, felt, and mesh samples, respectively). After scanning, each image stack was processed and visualized in the 3D data analysis application Dragonfly (Object Research Systems/ORS). Image stacks were segmented into pore space and stainless-steel skeleton regions of interest (ROIs) using the Otsu threshold method. The pore space ROI was used to develop a pore network model with the default settings in OpenPNM, an open-source plugin for pore size analysis hosted in Dragonfly ($\sigma=0.4$, R max =4, edge tolerance $= 0.10 \,\%$, and trim isolated pores enabled). Permeability values for each material were determined from fluidization data in our prior publication [57].

Frit samples 25-mm and 5-mm in diameter were then prepared for capillary flow porometry (CFP) and mercury intrusion porosimetry (MIP), respectively. These methods were chosen to compare the number of through-pores from CFP to the number of all open pores, which includes through-pores and dead-end pores, from MIP. Both techniques relate the fluid injection pressure P to the equivalent cylindrical pore size d_s through the Washburn equation,

$$d_s = -\frac{4\gamma_l cos\theta_l}{P} \tag{4}$$

where γ_l is the liquid surface tension and θ_l is the contact angle between the solid skeleton and intruded liquid. In MIP, the volume change of mercury intruded into the sample is monitored with a capacitance sensor to give a pore volume versus pressure curve. In CFP, pores are filled with wetting liquid and flow rate is monitored as the pores are emptied. The pore number density can be derived from the Hagen-

Poiseuille equation,

$$Q = -\frac{n_{d_s}\pi d_s^4 \Delta P}{128nl} \tag{5}$$

where Q is the fluid flow rate; n_{d_s} is the number density of pores with diameter d_s ; ΔP is the fluid pressure drop; η is the fluid viscosity; and l is the sample thickness.

Capillary flow tests were performed in a Quantachrome (brand of Anton Paar) 3Gzh Porometer. During flow tests, pressure drop across the sample was increased from zero to 0.2 bar to drive Porofil fluid (density $=1.85~\text{g/cm}^3$ surface tension =16~dyn/cm) through the solid skeleton. Both dry and wet curves were analyzed. MIP tests were conducted using a Quantachrome Poremaster 60 GT in low- and high-pressure modes (pressure range 0–60 psi) after running an ultimate vacuum of 3.0 µbar for 10 mins using a two-stage direct drive pump to remove sample moisture and contaminants.

Tortuosity of the porous media samples was derived from the segmented tomography image stacks using the free MATLAB application TauFactor. TauFactor performs a numerical diffusion simulation using voxels from the tomography data as mesh cell elements to compare the steady-state diffusive flow through the tomography-derived pore network to that of a perfectly dense control volume. The ratio of these flows gives the tortuosity of the porous media sample through the equation,

$$D^{eff} = D \frac{\varepsilon}{\tau} \tag{6}$$

where D is the intrinsic diffusivity of the void space. When applicable, tomography data sets were cropped to fall within a 1001-pixel cube (Table 2) to keep diffusion simulations under the 64 GB memory capacity of our lab workstation. TauFactor simulations were performed using the "(D:D) w/ Mirror" option. More details on the TauFactor algorithm and numerical implementation can be found in the software documentation [50].

Although all three frit materials are constructed of the same material (stainless steel), powder flow may also be affected by differences in local surface topology or the presence of surface species. Short-range cohesive forces are known to be particularly sensitive to surface properties such as nanoscale roughness [58–60] and chemical composition [61,62]. To evaluate whether powder-baseplate interactions are altered by the presence of an ALD-grown alumina film, 50 cycles of alumina were deposited on frit sample squares (\sim 0.25" x 0.25") that were compared to uncoated frit samples.

Flat ALD was performed in a 2-in. stainless steel reactor tube with a porous distributor plate. Nitrogen was used as the inert carrier gas and maintained at a flow rate of around 10 sccm. A vacuum pump held the reactor outlet pressure at 0.7 Torr. Liquid precursors trimethylaluminum (TMA, Sigma-Aldrich) and DI water were delivered as gaseous reactants from a vapor draw precursor delivery manifold held at 80 °C. Precursor bottles were maintained at 25 °C. After setting the reactor

Table 2 Dimensions, in pixels, of TauFactor image samples

Sample Name	Pixels in x	Pixels in y	Pixels in z
Powder	1000	1000	1000
Felt	1001	1001	292
Mesh	900	900	302

Table 1
List of CT microscope settings

Sample Name	Projections	Binning	Power (W)	Objective	Exposure (s)	Resolution (microns)	Image size L x W (pixels)
Powder	1996	1	9.94	4×	2	1.06	2026 × 1976
Felt	2401	1	10.08	4×	0.5	1.06	2026×2026
Mesh	2401	2	10.08	4×	0.6	5.97	1013×1013

temperature to 200 °C, the entire system was allowed to reach thermal equilibrium overnight before starting the ALD sequence. A typical ALD cycle comprised of a 3-min TMA dose followed by a 50-min nitrogen purge and a 1-min water dose followed by a 50-min nitrogen purge. Long nitrogen purges were chosen to ensure proper precursor and gaseous byproduct evacuation for the porous substrates at the low vacuum conditions (0.7 Torr) in the coating chamber before starting the next precursor dose. Reactor control and data acquisition were performed in a custom LabVIEW program. Scanning electron microscopy (SEM) with energy dispersive X-ray spectroscopy (EDS) was performed at the Colorado Shared Instrumentation in Nanofabrication and Characterization (COSINC) facility to confirm an increase in surface aluminum weight percent after 50 ALD cycles. The surface aluminum percent is determined by averaging the spatial (pointwise) aluminum distribution from EDS over the entire ~2-mm by 2-mm scan area. The spatial resolution of the JEOL JSM-7401F Field Emission SEM is roughly

The powder-baseplate cohesiveness for each frit material sample was analyzed using force-deflection ("pull-off" force) measurements in contact mode on a Bruker Icon atomic force microscope (AFM). A 10- μ m-diameter borosilicate colloidal AFM probe (Nanosensors, part number CP-qp-CONT-BSG) was purchased to act as a spherical contact point representing the Mo-Sci glass beads from the powder bed. Before evaluating sample pull-off force, the deflection sensitivity (171.2 nm/V) and spring constant (0.02176 N/m) of the probe were determined by calibrating against fused quartz and using the thermal tune calibration method, respectively. Five sites were measured on each sample and averaged to give a mean adhesive force.

2.3. Equations

Both the gas phase – a mixture of precursor, purge, and product gases – and the solid substrate phases for the frit and powder bed are treated as continua in this work. Rather than tracking each particle in the powder bed as a discrete entity, the entire powder bed is treated as a solid skeleton with continuum properties (Fig. 1). Individual particle quantities such as mass m_p , diameter d_p and number of sites $n_{s,\ p}$ become continuum properties of the packed bed i.e. solids density ρ_s , bed porosity γ , surface-to-volume ratio SV_s , site density ρ_{site} , and so on. In a porous media formulation, spatial variations in bed surface titration uniformity and precursor utilization can be tracked without the need to resolve individual particle behavior.

The reacting MPM model involves solving mass, momentum, (thermal) energy, and species balances. The conservation equations for mass and momentum used in this work are,

$$\frac{\partial \rho_m}{\partial t} + \nabla \bullet \left(\rho_m \vec{v}_m \right) = 0 \tag{7}$$

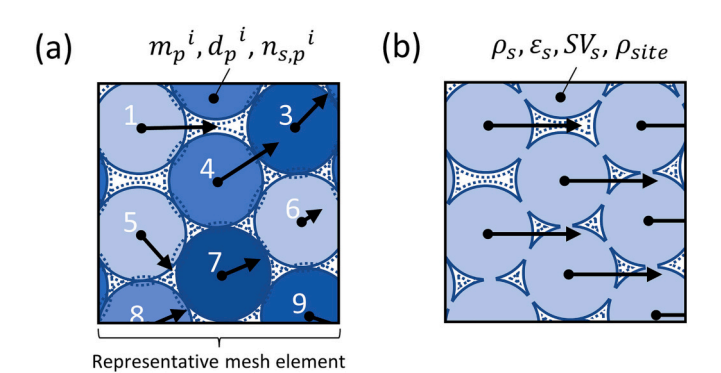


Fig. 1. (a) Schematic illustration of the traditional Lagrangian approach, where discrete properties of each particle i are tracked. (b) Porous media treatment, where the packed bed of particles is treated as a porous solid skeleton.

$$\frac{\partial}{\partial t} \left(\rho_m \vec{v}_m \right) + \nabla \bullet \left(\rho_m \vec{v}_m \vec{v}_m \right) = - \nabla P_m + \nabla \bullet \left(\vec{\tau}_m \right) + \rho_m \vec{g} + \vec{F}$$
 (8)

where ρ_m is the mixture density; \vec{v}_m is the mixture velocity; P_m is the static pressure of the mixture; τ_m is the mixture stress tensor; \vec{g} is the gravity vector; and \vec{F} is an external body force term. Laminar flow is assumed due to the low particle Reynolds numbers at typical CVR-ALD conditions ($Re_p{\sim}1$ or less). In porous media zones, porosity of the porous medium γ is added to the transient terms which become $\frac{\partial (\gamma p_m)}{\partial t}$ and $\frac{\partial \left(\gamma p_m \vec{v}_m\right)}{\partial t}$. \vec{F} accounts for the pressure drop due to viscous losses through the porous medium. The viscous loss term in each direction k, F_k , is described by,

$$F_k = -\mu_m C_{v,k} \left| \overrightarrow{v}_{m,k} \right| \tag{9}$$

where $C_{v, k}$ is the viscous resistance in direction k and $\left| \overrightarrow{v}_{m,k} \right|$ is the mixture velocity magnitude in direction k. Viscous resistance is also known as inverse permeability $1/\alpha_k$ with α_k being the permeability in direction k.

The heat transfer equation for the transport of thermal energy is described by,

$$\frac{\partial}{\partial t} \left(\rho_m e_{m,t} \right) + \nabla \bullet \left(\vec{v}_m \left(\rho_m e_{m,t} + P_m \right) \right) = \nabla \bullet \left(k_m \nabla T_m - \sum_j h_j \vec{J}_j + \vec{\tau}_m \right) \\
\bullet \vec{v}_m + S_h \tag{10}$$

where $e_{m,t}$ is the total energy of the mixture $(e_{m,t}=e_m+V_m^2/2)$; V_m is the scalar mixture velocity; e_m is the mixture internal energy $(e_m=C_{v,m}T_m)$; $C_{v,m}$ is the constant-volume heat capacity of the mixture; k_m is the mixture conductivity; T_m is the mixture temperature; h_j is the sensible heat of species j; \vec{J}_j is the diffusion flux of species j; and S_h is a thermal energy source term accounting for volumetric heat generation from chemical reactions. For incompressible flows, the total energy per unit mass can be related directly to the temperature by neglecting the pressure (P_m) and kinetic energy $(V_m^2/2)$ terms. In porous media regions where the fluid flow and porous medium are assumed to be in thermal equilibrium, thermal energy transport takes the form,

$$\frac{\partial}{\partial t}(\gamma \rho_m h_m + (1 - \gamma)\rho_s h_s) + \nabla \bullet \left(\rho_m \vec{v}_m h_m\right) = \nabla \bullet \left(k_{eff} \nabla T_m\right) + S_h \tag{11}$$

where h_m is the mixture enthalpy; ρ_s is the solid material density; h_s is the sensible enthalpy of the porous medium; k_{eff} is the effective thermal conductivity ($k_{eff} = \gamma k_m + (1 - \gamma)k_s$); and k_s is the solids conductivity.

The transport of chemical species is modeled using the Fickian convection-diffusion equation with volumetric (CVD) and wall surface (ALD) reactions,

$$\frac{\partial}{\partial t}(\rho_i Y_i) + \nabla \bullet \left(\rho_i \vec{v}_m Y_i\right) = -\nabla \bullet \vec{J}_i + R_i \tag{12}$$

where ρ_i is the density of chemical species i; Y_i is the mass fraction of i; \vec{J}_i is the diffusion flux of species i; and R_i is the generation rate of i due to chemical reactions. N-1 chemical species transport equations are solved, where N is the number of species; the N^{th} mass fraction is calculated as $1-\sum_{j}^{N-1}Y_j$. In porous media zones, the transient term includes porosity, becoming $\frac{\partial}{\partial t}(\gamma \rho_i Y_i)$. The diffusion flux is modeled with the dilute approximation,

$$\vec{J}_i = -\rho_i D_{i,m} \nabla Y_i - D_{T,i} \frac{\nabla T_m}{T_m} \tag{13}$$

where $D_{i, m}$ is the mass diffusivity of species i and $D_{T, i}$ is the thermal (Soret) diffusivity of i.

Finite-rate kinetics with no turbulence-chemistry interaction (TCI) contribute to the net source of chemical species i, R_i , according to the following relation,

$$R_{i} = M_{w,i} \sum_{1}^{N_{r}} \left(\nu_{f,ir} - \nu_{b,ir} \right) \left(k_{f,r} \sum_{1}^{N_{j}} \left(C_{j} \right)^{\eta_{j,r}} - k_{b,r} \sum_{1}^{N_{j}} \left(C_{j} \right)^{\eta_{j,r}} \right)$$
(14)

where $M_{w,\;i}$ is the molecular weight of species $i; v_f, i_r$ and v_b, i_r are the product and reactant stoichiometric coefficients in reaction $r; k_f, r$ and k_b, r are the forward and reverse rate constants for reaction $r; C_j$ is the molar concentration of species j; and η_j, r is the rate exponent of species j in reaction r, all summed over N_j chemical species and N_r chemical reactions. Species concentrations in the reaction rate expression above can include gas-phase species, surface-adsorbed site species, or solid film deposition species.

In this work, the forward reaction rate constant, k_f , r, is defined using the Arrhenius equation with no temperature term and with site coverage dependence,

$$k_{f,r} = A_r e^{-E_{a,r}/(R_g T_m)} \prod_{k,m} Z_k^{\mu_{k,r}}$$
(15)

where A_r is the Arrhenius pre-exponential factor or "prefactor"; $E_{a,\ r}$ is the activation energy for reaction r; R_g is the universal gas constant; Z_k is the fraction of sites covered by site species k ($Z_k = C_k/\rho_{site}$); C_k is the concentration of site species k; ρ_{site} is the constant surface site density; and $\mu_{k,\ r}$ is the site coverage rate exponent. For CVD volume reactions, the surface coverage term drops out ($\mu_{k,\ r}=0$). The Arrhenius prefactor for heterogeneous reactions with a first-order dependence on the concentration of gas species i can be calculated using $A_r = \lambda \sqrt{R_g/(2\pi M_{w,i})}$ where λ is the sticking coefficient [63].

In moving mesh zones, the integral form of each conservation equation over a control volume *V* utilizes a relative velocity formulation,

$$\frac{\partial}{\partial t} \int_{V} \rho_{m} \phi dV + \int_{\partial V} \rho_{m} \phi \left(\vec{v}_{m} - \vec{v}_{dm} \right) \bullet d\vec{A} = \int_{\partial V} \Gamma_{\phi} \nabla \phi \bullet d\vec{A} + \int_{V} S_{\phi} dV$$
 (16)

where ϕ is a scalar quantity described by a conservation equation; \vec{v}_{dm} is the moving mesh velocity; Γ_{ϕ} is the diffusivity of quantity ϕ ; and S_{ϕ} is the total generation rate of ϕ from sources and sinks. Details on the moving mesh numerical implementation can be found in the Fluent theory manual [39].

2.4. Reactor modeling

CFD-DEM simulations have shown that the porosity and coordination structure of the packed bed under vibratory convection do not change significantly when subjected to low vertical accelerations [57]. In this regime, the powder bed can be considered to move as a continuum. The mean powder bed convection velocity at a vertical acceleration of 0.30g, where g is the magnitude of the gravity vector, was approximated as a piecewise velocity profile in this work. The contact region is fit to the sinusoidal conveyor velocity and a constant horizontal liftoff velocity was chosen that gives the same average powder bed velocity as the experimental results, $\overline{u}_{pb}=1.3$ cm/s (Fig. 2). The resulting piecewise velocity is prescribed to the packed bed zone in the MPM model.

ANSYS Fluent was chosen to model the CVR-ALD system as one of the few CFD packages with heterogeneous surface reactions, porous media, and moving mesh capabilities already built in. A mixture model was applied to the gas phase. Five volumetric (gas) chemical species were considered in this work: (1) the aluminum containing precursor, trimethyl aluminum (tma/alme3); (2) the oxidizing precursor, water (h2o); (3) the inert carrier gas, nitrogen (n2); (4) the ALD byproduct,

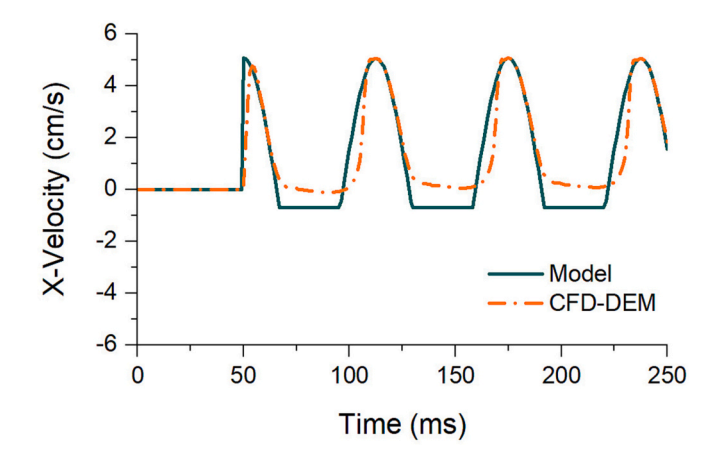


Fig. 2. Comparison between the CFD-DEM mean powder convection velocity (dash-dot) and the piecewise model approximation with the same average powder bed velocity as the experimental results (solid line).

methane (ch4); and (5) a CVD byproduct, aluminum hydroxide (al(oh)3) [64]. Aluminum hydroxide was chosen so that the CVD byproducts could be monitored separately from the ALD-deposited alumina. Two site species (surface hydroxyls, oh, and an alumina intermediate, oal (ch3)2) and one solid film species (alumina, al2o3) were also considered. The mixture model and porous media properties can be found in Table 3. Standard state enthalpies and entropies were obtained from the NIST Chemistry WebBook when available [65]. Material properties not defined in Table 3 were left at the Fluent Database defaults. Viscous resistances were calculated using the inverse permeability from pressure drop versus gas velocity fluidization data [57]. Site density was determined assuming a surface site area of 24 nm² [8]. The remaining porous media properties for the frit (surface-to-volume ratio and porosity) were derived from segmented tomography images. All reactions were modeled as irreversible ($k_{b, r} = 0$) with a temperature-independent forward reaction rate constant ($E_{a, r} = 0$). ALD Arrhenius prefactors were calculated by incorporating a constant reactor temperature with a sticking probability of $\lambda = 0.01$ (i.e., $A_r = \lambda_1 / R_g(473) / (2\pi M_{w,i})$) [8].

Three reactions were modeled in the CVR-ALD reactor: a monodentate-type TMA half-reaction [66,67], a water half-reaction, and a CVD reaction producing aluminum hydroxide [64,68]. These were described by the following equations,

$$\|-OH + Al(CH_3)_3 = CH_4 + \|-OAl(CH_3)_2$$
(17)

$$2\| - OAl(CH_3)_2 + 3H_2O = 4CH_4 + Al_2O_3 + 2\| - OH$$
 (18)

$$Al(CH_3)_3 + 3H_2O = 3CH_4 + Al(OH)_3$$
(19)

The ALD reactions are modeled as first order in concentration and coverage dependence. The CVD reaction is modeled as second order in concentration dependence (η_{TMA} , $_3=1$ & η_{H_2O} , $_3=1$). All porous materials were assumed to start with fully hydroxylated surfaces ($\parallel -OH$ site coverage =1).

Two geometries were used to model the CVR-ALD reactor in this study: a "single zone" model describing the region corresponding to one precursor and a "single cycle" model containing two precursor zones to describe a single cycle of ALD (Fig. 3). In both models, the frit zone thickness is 1.59 mm and the packed bed zone thickness is 3 mm. The single-zone model only contains three volumetric species (ch4, n2, and alme3 or h2o) while the single-cycle model contains all species from Table 3. Because only one precursor region is included, CVD reactions are not considered in the single-zone model. In all models, periodic boundary conditions were applied to the left and right boundaries. Inlets and outlets were set to the mean reactor temperature (473 K). The fluid zones at each outlet were split at the last two rows of mesh cells so that

Table 3Simulation values

Fluid properties								
	Nitrogen	Methane	TMA	Water	-OAl (CH ₃) ₂	-OH	Al ₂ O ₃	Al(OH) ₃
Standard state enthalpy [J/kgmol]	0	-7.49e+07	-8.49e+07	-2.42e+08	-1.50e+08	3.90e+07	3.90e+07	2.59e+08
Standard state entropy [J/kgmol-K]	1.91e+05	1.86e+05	3.50e+05	1.89e+05	5.09e+04	1.84e+05	1.84e+05	1.88e+05
Molecular weight [kg/kmol]	28.01	16.04	72.09	18.02	73.05	17.00	102.00	78.03
* Mixture settings were assigned default values (incompressible ideal gas for density, mixing law specific heat, and constant values for thermal conductivity, viscosity, and mass diffusivity)								
Solid (porous media) properties								
	Glass	Stainless- steel						
Density, ρ_s [kg/m3]	2500	8030						
Specific heat, c_p [J/kg-K]	871	503						
Thermal conductivity, k_s [W/m-K]	1.3	16.3						
Chemical reactions								
	TMA half-	H ₂ O half-	CVD					
	reaction	reaction	reaction					
Arrhenius prefactor, A_r [1/s]	0.9	1.9	1.0					
Species with $\eta_{j, r} = 1$	TMA	H_2O	TMA, H_2O					
Species with $\mu_{k, r} = 1$	∥ − <i>OH</i>	\parallel - AlO $(CH_3)_2$	N/A					
* Reaction settings were assigned default values (heat of surface reactions enabled, diffusion energy source enabled, direct source chemistry solver)								
Cell zone and boundary conditions, all								
Vibration y-amplitude [g]	0.30							
Vibration frequency [Hz]	16							
Vibration angle [°]	60							
Liftoff y-velocity [cm/s]	-0.40							
Precursor velocity [cm/s]	3–4							
Precursor mass fraction	0.001							
Purge velocity [cm/s]	3–4							
Reactor temperature [K]	473							
Cell zone conditions, porous zones only								
,		Packed bed	Frit					
Surface-to-volume ratio [m ⁻¹]	58,000	100,000						
Site density [kgmol/m ²]	6.92e-11	6.92e-11						
Solid material		glass	stainless-					
			steel					

the backflow species mass fractions could be assigned to area-averaged values from the near-outlet cells. As ALD progresses, reaction byproducts begin populating the outlet stream, so a time-dependent backflow mass fraction condition more accurately represents the transient composition of the outflowing gas.

Reactor vibration is incorporated through user-defined functions (UDFs). Two DEFINE_ZONE_MOTION UDFs were developed to describe the vibrating reactor and vibrating-conveying packed bed, respectively. These two mesh zones slide across one another in the horizontal direction. Mesh interfaces were created at faces joining the three cell zones (fluid, packed bed, and frit regions). DEFINE_CG_MOTION UDFs at the packed bed inlet and outlet maintain alignment between the packed bed boundaries and the reactor boundaries. Dynamic meshing is only needed at the packed bed inlet and outlet faces, where the mesh cells must be relayered to account for packed bed convection from left to right. Layering was enabled with the recommended settings (height-based, split factor = 0.4, collapse factor = 0.4). Cell height was assigned a value roughly corresponding to the peak-to-peak vibration amplitude (0.00034 m) so that one remeshing step occurs after one period of vibration.

The resulting system of equations was solved using Fluent's transient, pressure-based solver. A converged solution was obtained using the

SIMPLE algorithm with pressure-velocity coupling and Rhie-Chow distance-based fluxes. Default values were retained for the under-relaxation factors (0.3 for pressure, 0.7 for momentum, and 1 for all other equations). The gas flow field was allowed to equilibrate for 50 ms before vibration was turned on.

3. Results and discussion

3.1. Porous media properties

Before running any CVR-ALD simulations, the microstructural characteristics of three candidate frit materials marketed as 10- μ m porous media were evaluated. We were interested in how the internal pore structure may affect permeability and the total surface area available for ALD reactions. Tomography data of the frit materials reveals differences in connectivity and pore shape among all three pore networks (Fig. 4). The sintered powder sample is characterized by amorphous, highly interconnected pores (Fig. 4a). Pore path diameters in the pore network model vary from short, <10- μ m diameter segments to wide 74- μ m diameter channels. Pore vertices of varying size are distributed uniformly throughout the sintered powder with sizes from 67 μ m down to <10 μ m. The sintered felt sample has similar

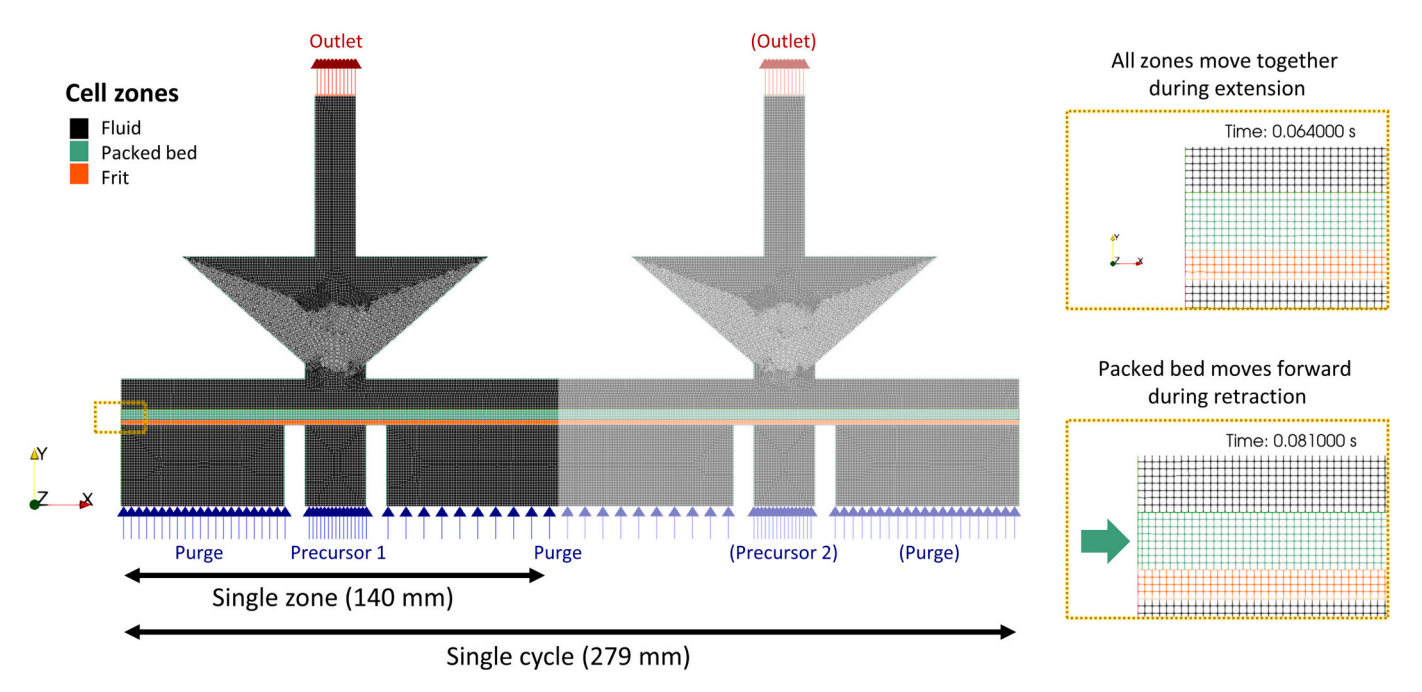


Fig. 3. Simulation setup (left) for the single-zone model with 49,748 mesh elements and the single-cycle model with 99,432 mesh elements. Insets display sample snapshots of the moving mesh during extension (right, top) and retraction (right, bottom) as the packed bed zone (green) slides to the right over the frit zone (orange). (For interpretation of the references to colour in this figure legend, the reader is referred to the web version of this article.)

interconnectivity and pores spanning a similar size range but with different spatial distributions (Fig. 4b). The sintered felt material is functionally graded through the thickness so pore vertices range from 21 μ m to <10 μ m with larger pores concentrated at the bottom face in Fig. 4b. Pore path diameters are also shorter and range from <10 μm to 25 µm in size. The sintered mesh material exhibits larger spatial pore network variations and more noticeable geometric anisotropy than the felt and powder samples (Fig. 4c). Very large pores up to $614 \mu m$ in size are visible concentrated at the bottom face in Fig. 4c within the two coarsest mesh layers. The top three mesh layers are dominated by pores <100-μm in size. The wide distribution in pore sizes for the multilayer mesh material is by design. A coarse mesh underlayer permits low pressure drops and imparts structural integrity to the mesh while the fine mesh overlayer prevents fines from passing through the porous material. Pores in the bottom half of the mesh also appear less interconnected than the dense pore networks of Fig. 4a and b. Pore path diameters are also larger for this material, ranging from 601 μm to <20 μm through the finest mesh layer.

Similar trends are observed in the porometry and porosimetry results (Fig. 5). The powder, felt, and mesh sintered samples are characterized by mean through-pore sizes of 12.32, 16.08, and 20.12 μm , respectively. MIP results from Fig. 5b and the tomography data from Fig. 4a indicate that the sintered powder has more large open pore spaces than the felt, but only a fraction of the pore regions constitutes through-pores. The mean through-pore size, not the average size of all pores, is most relevant to experimental flow measures such as CFP. However, it should be noted that dead end pore spaces still provide additional surface area containing reaction sites that can be accessed by ALD precursors through diffusion. The overlap between MIP and CFP results gives a qualitative indication of the dead-end pore frequency. The felt results have the most overlap with only a few small <12- μ m and large >25- μ m pores observed in the MIP results that were not seen in the CFP results. The powder results overlap mostly for the small pores sizes with a significant number of pores 20–50 μm not seen in the CFP experiments. Many large >50- μm pore spaces can be seen in the mesh MIP results that are not detected in CFP. This is consistent with the tomography data from Fig. 4c indicating that large pores are present in the bottom half of the sintered mesh material, but that flow must pass through small pores in the finest mesh

layer before exiting the sample.

To better understand how the geometric anisotropy and pore interconnectivity trends observed in Fig. 4 affect material permeability, tortuosity factors for in-plane flow (τ_1^2 and τ_2^2) and through-plane flow (τ_3^2) were obtained from TauFactor simulations (Fig. 6). The most highly interconnected pore network from Fig. 4 (the sintered powder) had the highest tortuosity factors. The sintered felt material was characterized by the lowest tortuosity factors. Although the sintered felt pore network is also highly interconnected, the porosity is higher, leading to shorter effective pore paths. In general, all materials were only marginally anisotropic in terms of flow resistance - tortuosity factors τ_1^2 , τ_2^2 and τ_3^2 for the sintered powder and sintered felt were within 0.1-0.3 of one another. Tortuosity values typically decreased with increasing porosity, a trend consistent with common tortuosity correlations such as the 2D fiber Tomadakis [69] model and the Bruggeman [70] model. Only the mesh tortuosity results exhibited noticeable anisotropy with a through-plane tortuosity factor τ_3^2 around 0.7 lower than the in-plane tortuosity factors τ_1^2 and τ_2^2 .

The TauFactor and XRCT porous media properties in Table 4 were used in eq. 1 with the experimental permeability values to determine the fitted KC constant c_0 . Porosity and specific surface area were calculated from the segmented XRCT images. Approximate porous media properties for the packed bed of 56-µm glass particles are provided for comparison. Permeabilities followed the same order as the mean throughpore size; the sintered powder was the least permeable material followed by the sintered felt and the sintered mesh. However, the fitted KC constants did not follow the same trend as the through-plane tortuosity factors τ_3^2 , indicating significant differences in pore shape factor c.

Several arguments can be made to explain why the KC constants for the sintered felt and sintered mesh samples deviated significantly from the default value of five [48,71]. The specific surface areas in Table 4 are calculated from the XRCT images by taking the surface to volume ratio of rectangular prisms forming voxels [50]. This discontinuous, pixelized representation may be a poor approximation of the true pore surface. Specific surface area has a power law relationship with permeability so any errors in surface area are magnified in the permeability equation. Reported KC constants exceeding five are also not uncommon for

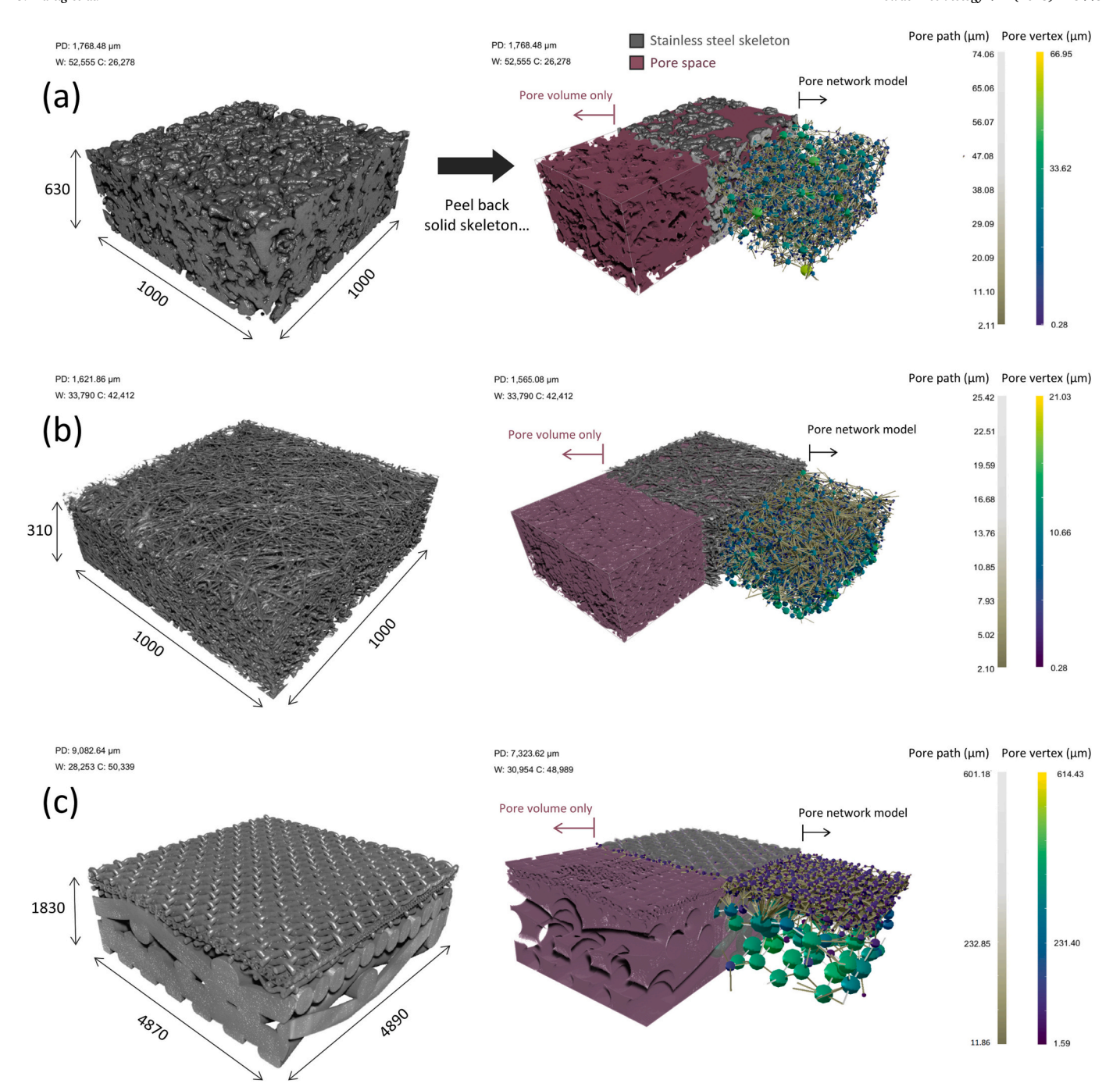


Fig. 4. XRCT results for three sintered stainless steel baseplate materials: (a) sintered powder, (b) sintered felt, and (c) sintered mesh. 3D visualizations of tomography data display dimensions rounded to the nearest $10 \mu m$ (left). The pore volume rendering and pore network model generated by OpenPNM are cropped and revealed by peeling back the solid skeleton (right).

anisotropic void spaces, particularly as the porosity increases beyond 0.4 [43]. Deviations from the Kozeny-Carman model have been attributed to unusable porosity [45,72] and unresolved complexities in the shape and interconnectivity of pore channels [55]. The Kozeny-Carman relationship assumes that the porous media can be approximated as a collection of sinuous but parallel identical round pipes [41]. For complex pore geometries, this treatment of porous media flow may be an oversimplification. Additional losses not accounted for in the base Kozeny-Carman model are expected accompanying sudden expansion and contraction of pore capillaries [55] which may explain the lower mesh permeability results.

Porous media surface topography can also influence the cohesive

force between the powder bed and the frit surface. In this study, no significant differences were detected between the three frit materials for the ALD-coated and uncoated samples (Fig. 7b). AFM pull-off force tests on all three frit materials were characterized by low adhesion values relative to other literature studies [73,74] from 4.7 to 13.2 nN in magnitude. Standard deviations increased with adhesion force magnitude from 2.1 nN for the ALD-coated mesh to 11.2 nN for the uncoated felt. The large pull-off force variations between replicates can be attributed to site-to-site differences in local surface topology and changes in contact area between the probe and the porous media sample. The presence of TMA-deposited aluminum was confirmed by the 1.2–1.4% weight increase in surface aluminum composition (Fig. 7a).

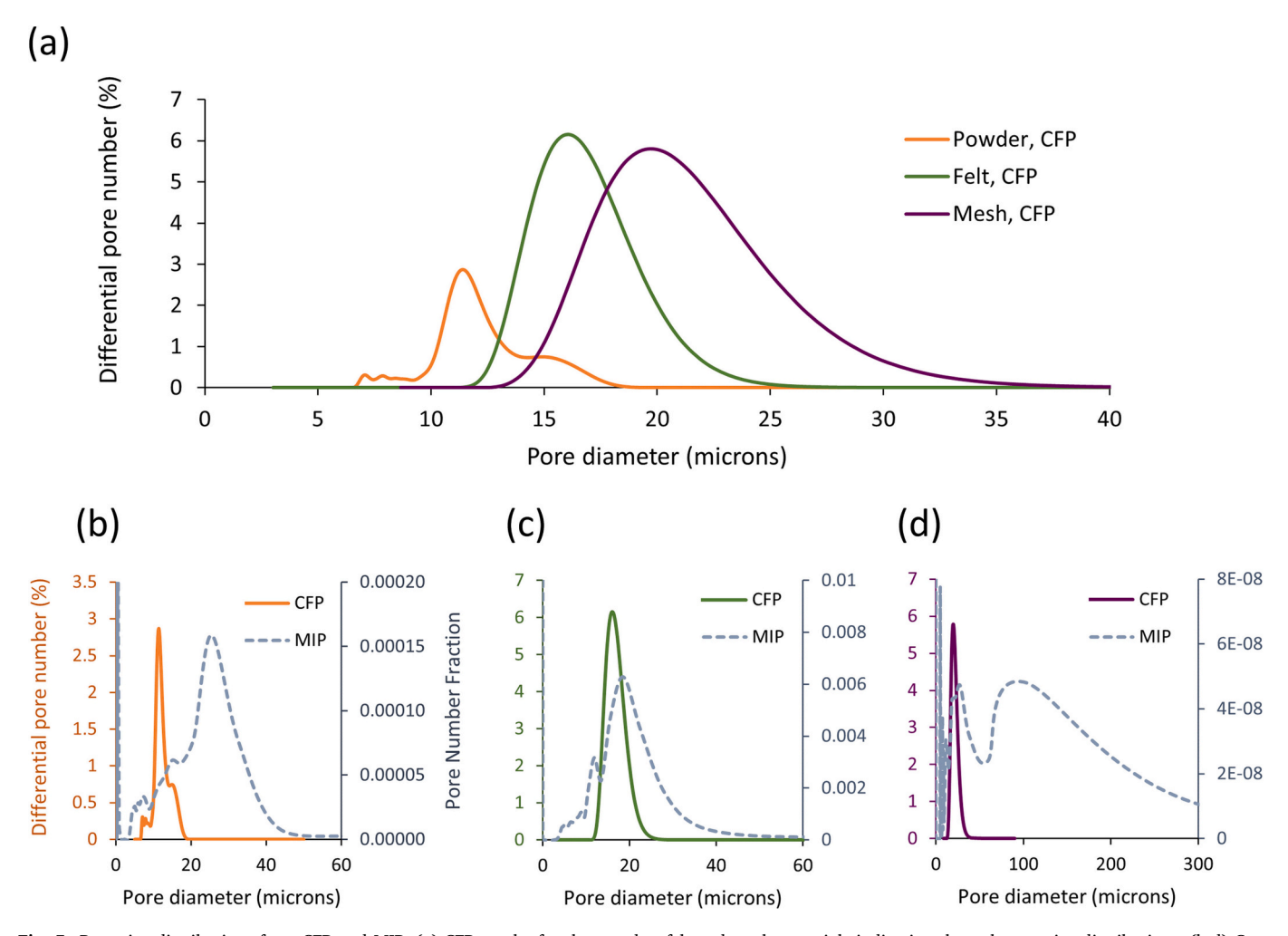


Fig. 5. Pore size distributions from CFP and MIP. (a) CFP results for the powder, felt and mesh materials indicating through-pore size distributions. (b-d) Comparisons between CFP (left y-axis) and MIP (right y-axis) results for the powder, felt, and mesh materials.

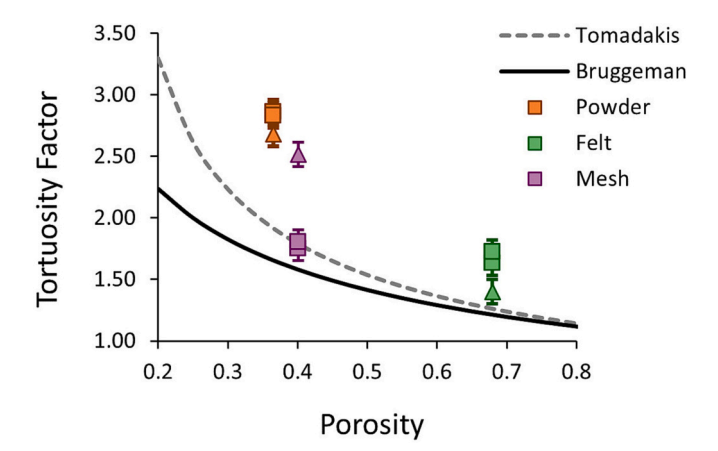


Fig. 6. In-plane (square points) and through-plane (triangular points) tortuosity factor versus porosity for all three sintered materials. The Tomadakis model was fit with parameters $\varepsilon_p = 0.11$ and $\alpha = 0.521$ for in-plane tortuosity or $\alpha = 0.785$ for through-plane tortuosity [69,71].

Further tests would be needed to confirm whether particle-frit cohesion is still insensitive to the presence of an ALD film for a thicker coating (>50 cycles alumina).

Table 4Porous media characterization results from analysis of fluidized bed data (for permeability) and XRCT images (all others). Specific surface area by total volume and by solid volume are included for ease in comparison with other studies

Value	Glass beads	Powder	Felt	Mesh
Porosity, ε	0.46	0.37	0.68	0.40
Tortuosity factor, τ_1^2	1.48*	2.86	1.63	1.75
Tortuosity factor, τ_2^2	1.48*	2.83	1.72	1.80
Tortuosity factor, τ_3^2	1.48*	2.68	1.40	2.52
Specific surface area, s_{ν} [μm^{-1}]	0.134†	0.097	0.194	0.011
Specific surface area, $S [\mu m^{-1}]$	0.073	0.062	0.062	0.007
Fitted KC constant, c_0	4.2	4.6	22.0	79.9
Permeability, $k [\mu m^{-2}]$	4.25	2.76	3.66	17.93

†Estimate assuming nearly spherical beads with sphericity $\phi_s=0.80$ ($s_v=6/(\phi_s d_s)$)

* Estimate from the Bruggeman correlation, $\tau^2 = \varepsilon^{-0.5}$

3.2. Multiphase flow behavior during CVR-ALD, single precursor zone

Reactor-scale CVR-ALD simulations revealed complex multiphase flow behavior during reactor operation. Vibration produced large, transient fluctuations in the flow streamlines relative to the flow behavior before vibration was turned on (Fig. 8). Vibration strength is expressed as a throw number Γ where Γ is the vertical vibration acceleration normalized by the magnitude of gravity g. For $\Gamma=0.30$ to $\Gamma=0.60$, the reactor vibrates at velocities exceeding the inlet gas velocity. As the extension stroke begins, flow transitions from primarily inlet-to-

J. Hartig et al. Powder Technology 421 (2023) 118448

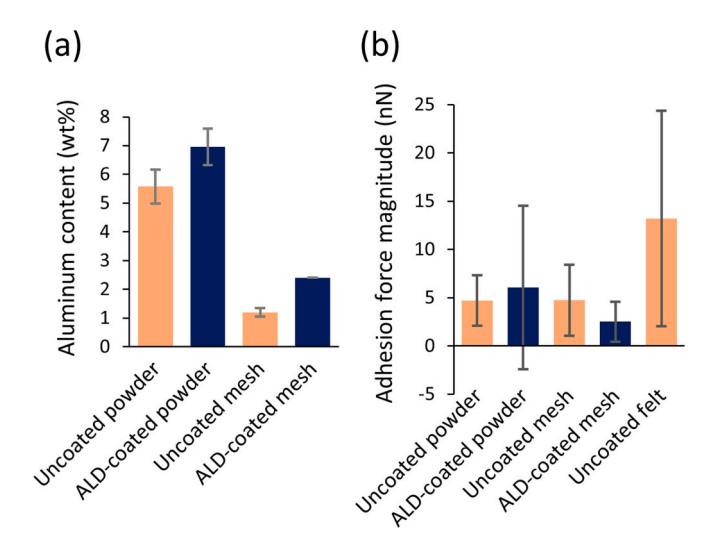


Fig. 7. (a) EDS aluminum surface weight percent results for coated and uncoated sintered porous media samples. (b) AFM adhesion force magnitude results for coated and uncoated sintered porous media samples.

outlet travel to left-right motion as the fluid moves with the reactor. During retraction, streamlines flip to predominately right-left motion. Some outlet gas is drawn into the reactor during the retraction stroke, but a similar volume of gas is expelled during extension. The symmetric, sinusoidal nature of the vibration prevents outlet gases from conveying into the reactor headspace. Similar behavior is observed between $\Gamma=0.30$ and $\Gamma=0.60$ but with larger transient fluctuations and more horizontal streamlines during extension and retraction.

The net effect of many vibration cycles is to spread out the precursor front (Fig. 9a, b). Maintaining the average packed bed velocity \overline{u}_{pb} constant, the TMA front can be seen extending farther into the head-space when $\Gamma=0.60$ than when $\Gamma=0.30$. The diffusive effect of vibration magnitude moves the TMA front within the packed bed closer to the packed bed inlet when $\Gamma=0.60$ than when $\Gamma=0.30$. Higher

vibration magnitudes lead to a shallower concentration gradient and more spillover into the purge zone headspace. An even more drastic effect is seen when increasing the average packed bed velocity from $\overline{u}_{pb}=0.5~cm/s$ to $\overline{u}_{pb}=3.0~cm/s$ while maintaining a constant vibration magnitude of $\Gamma=0.30$ (Fig. 9c and d). Packed bed convection is observed to have a "dragging" effect on the precursor concentration in both the headspace and the packed bed. The TMA front is pulled towards the outlet as entering hydroxylated particle surface sites consume the incoming TMA. Vibration magnitude and powder bed convection speed are directly correlated [26,75] but their functional relationship may also depend on particle size and bulk powder bed density so it is important to understand the effects of both factors independently.

The trends described in Figs. 8 and 9 can be quantified by comparing the average surface titration uniformity in the zone leading up to the centerline of the precursor inlet (Fig. 10a). The base case corresponding to the convection speed of 56- μm glass particles when $\Gamma=0.30$ is shown as a black dashed line in Fig. 10b. Higher vibration magnitudes allow the precursor front to spread faster within the packed bed, giving higher average surface titration values. Faster bed convection pushes incoming TMA towards the packed bed outlet and the subsequent water zone. Purge zones become more important for higher packed bed convection speeds and vibration magnitudes to prevent precursors from coming into contact.

Precursor mass fractions spanning two orders of magnitude were tested to evaluate how precursor concentration affects the average titration extent and the position of the reaction front (Fig. 11). Only a thin region near the surface of the powder bed in the $Y_{TMA}=0.0001$ case where $\gamma<1$ did not achieve full surface titration before exiting the TMA zone. The fast kinetics of the TMA half-reaction and low surface area of the GL56 powder bed ($<1~{\rm m}^2/{\rm g}$) enable high surface titrations even for mass fractions well below the TMA vapor pressure. Under these conditions, titration uniformity is limited by the number of TMA molecules available for reaction rather than the reaction rate.

The position and angle of the reaction front are established by a dynamic balance between the precursor flow and the influx of uncoated particles. Excess number γ [76,77] (a ratio between the number of precursor molecules in the reactor and the number of surface sites

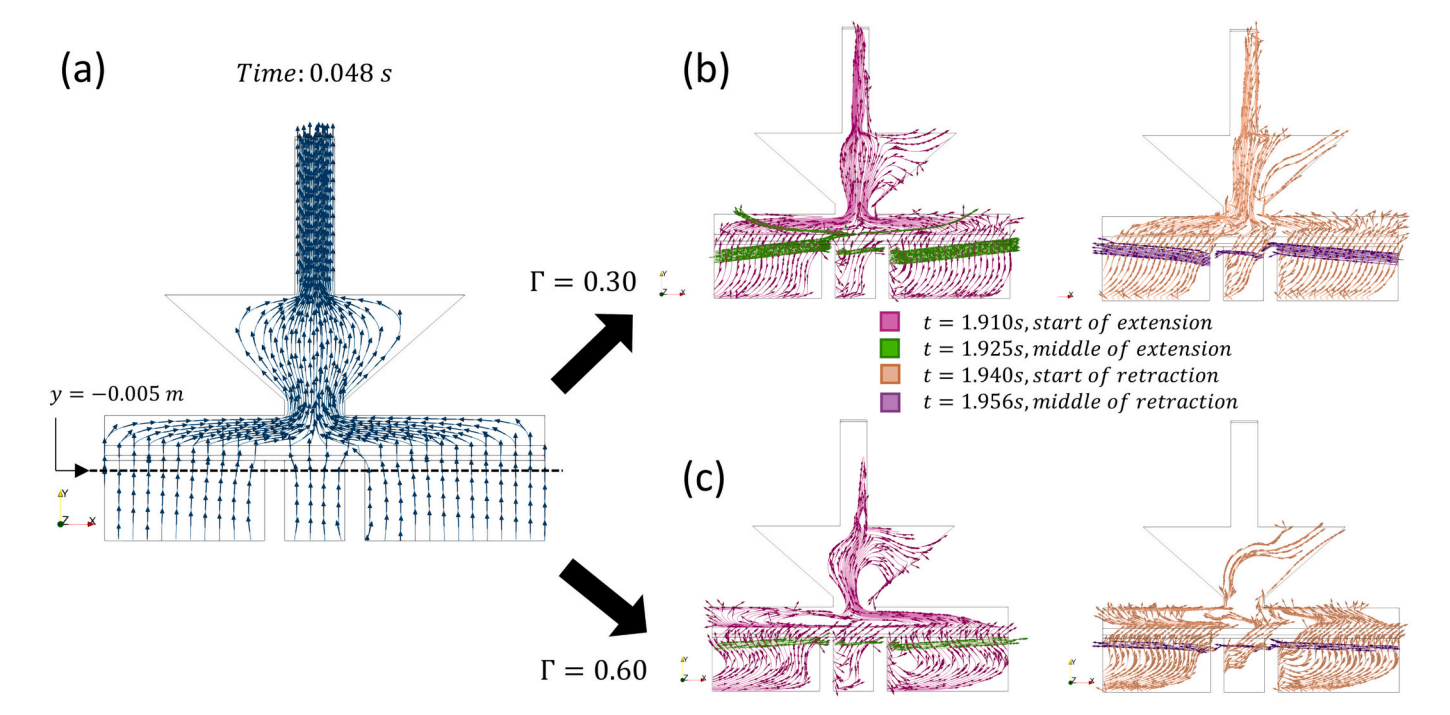


Fig. 8. (a) Steady streamlines for flow passing through the line y = -0.005 m (right below the frit, as shown) just before vibration is turned on. (b) Streamlines at select points during vibration when $\Gamma = 0.30$. (c) Streamlines at select points during vibration when $\Gamma = 0.60$.

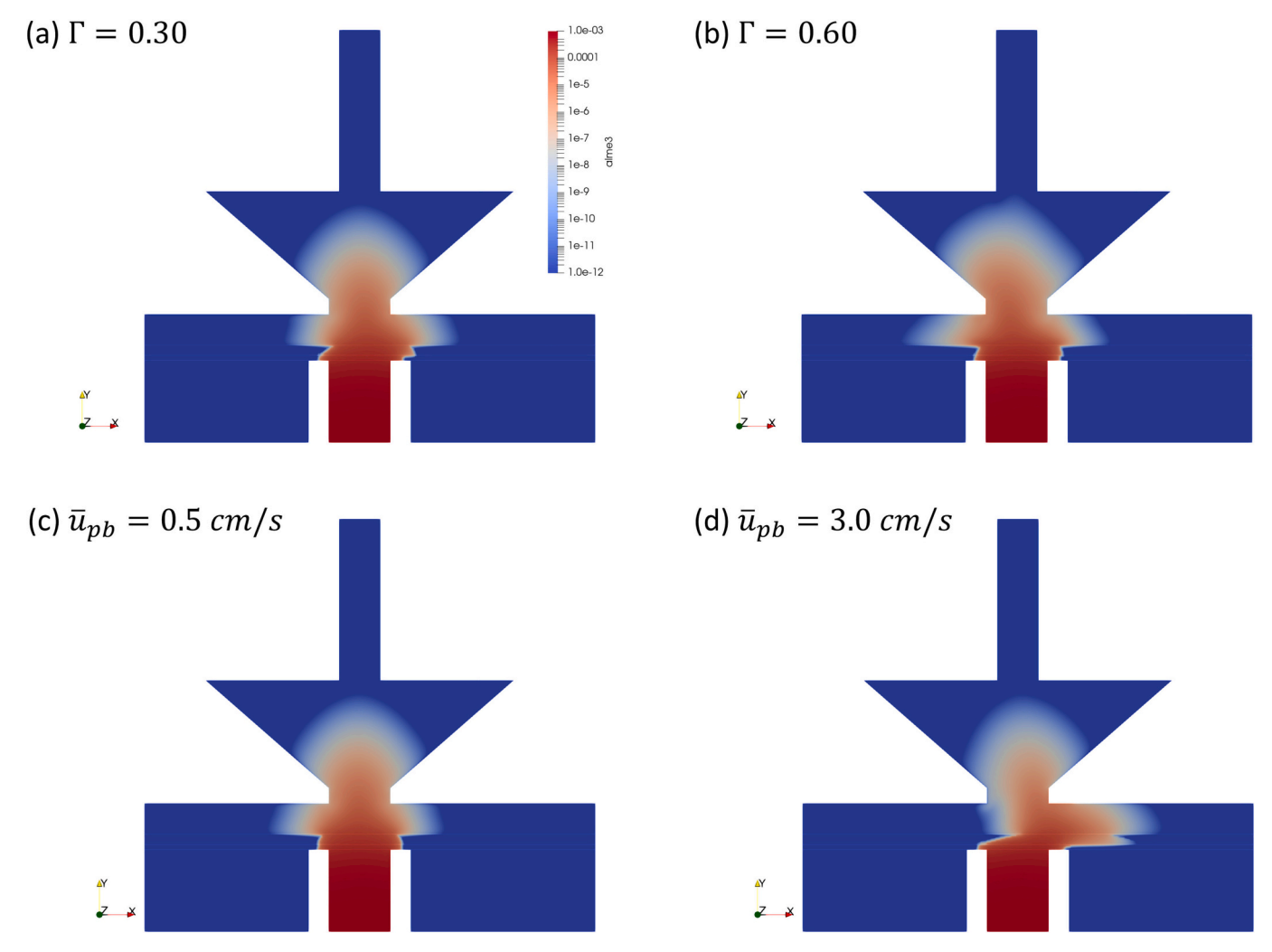


Fig. 9. TMA concentration profiles at t=1.925s (30 cycles of vibration) under different conditions. (a, b) Vibration magnitude Γ is adjusted while keeping the average packed bed velocity, \overline{u}_{pb} , constant by adjusting the packed bed liftoff velocity as discussed in Fig. 2. (c,d) Average packed bed velocity \overline{u}_{pb} is adjusted by increasing the liftoff velocity while keeping the vibration magnitude constant at $\Gamma=0.30$

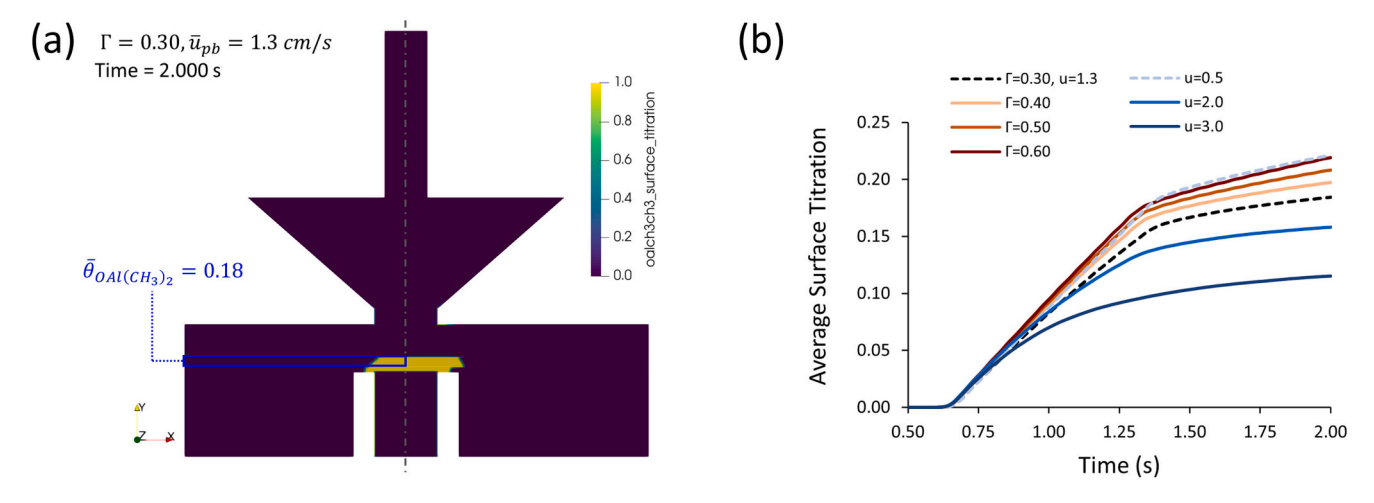


Fig. 10. (a) Blue boxed region of packed bed used to determine the average surface titration uniformity as quantified by the sterically hindered surface coverage of $OAl(CH_3)_2$, $\overline{\theta}_{OAl(CH_3)_2}$, (b) Average surface titration over time for four different vibration intensities while $\overline{u}_{pb}=1.3$ cm/s ($\Gamma=0.30$, 0.40, 0.50 & 0.60) and four mean powder bed convection velocities while $\Gamma=0.30$ ($\overline{u}_{pb}=0.5, 1.3, 2.0 \& 3.0$ cm/s) (For interpretation of the references to colour in this figure legend, the reader is referred to the web version of this article.)

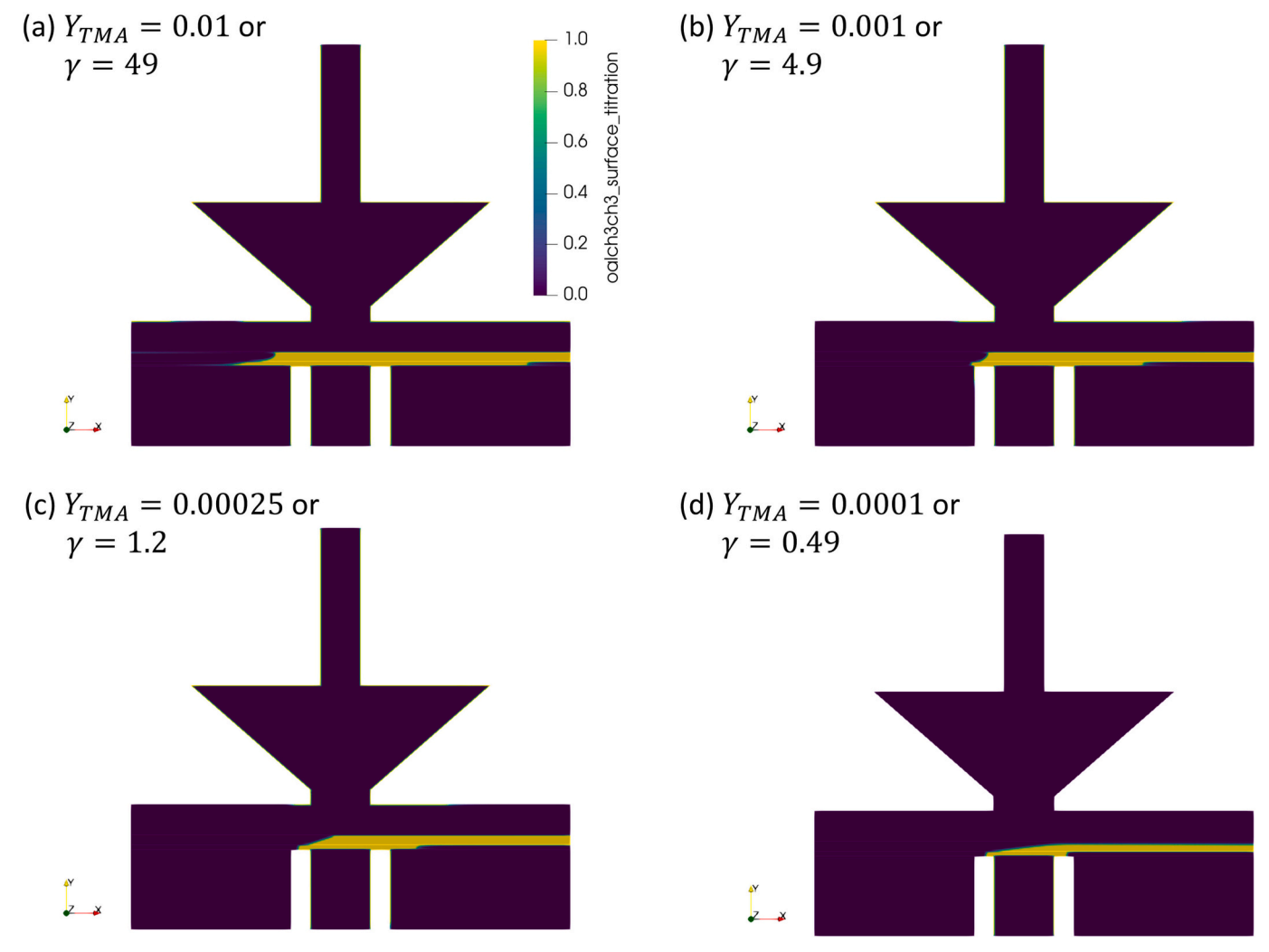


Fig. 11. Quasi-steady surface titration results for the TMA zone at t = 20 s for different precursor mass fractions or excess numbers

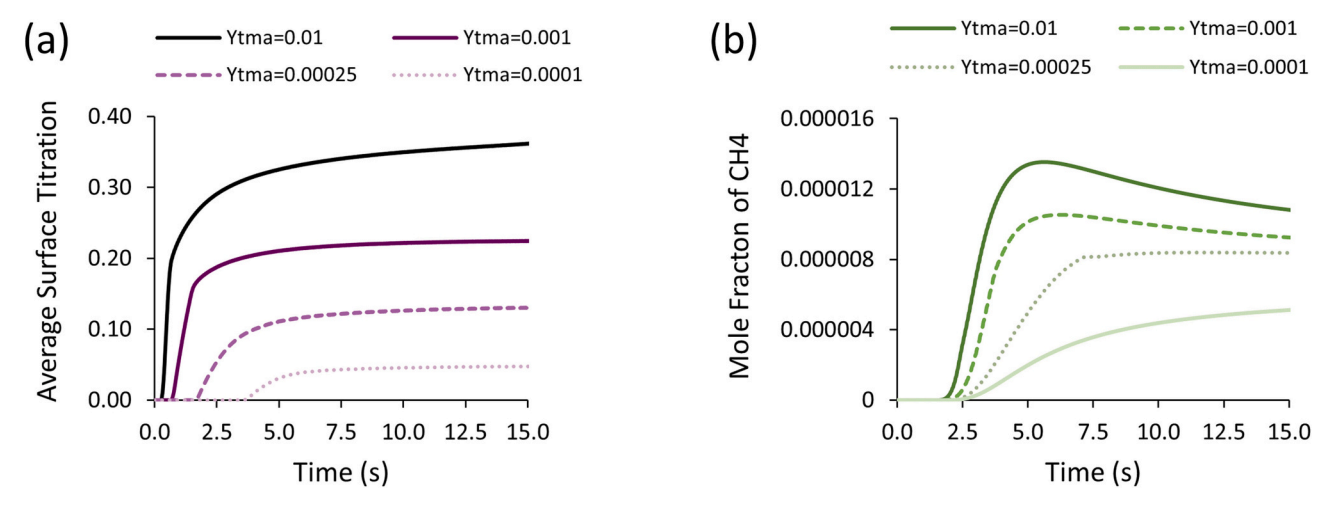


Fig. 12. (a, b) Average surface titration over the blue boxed region from Fig. 10a and mole fraction of methane at the reactor outlet over time for different precursor mass fractions in the precursor dosing region from Fig. 11 (For interpretation of the references to colour in this figure legend, the reader is referred to the web version of this article.)

available for ALD) can be used to quantify precursor excess. Redefining excess number on a molar flow rate basis gives,

$$\gamma = \frac{\dot{n}_{precursor}}{\dot{n}_{sites}} = \frac{v_g * w_{pr} * n_o * s_0}{\overline{u}_{pb} * h_{pb} * s_{rv}}$$
(20)

where v_g is the gas velocity ($\left|\overrightarrow{v}_m\right|$ from eq. 7); w_{pr} is the horizontal width of the precursor inlet; n_o is the inlet precursor concentration; s_0 is the surface site area; and h_{pb} is the height of the packed bed. The precursor inlet width, gas velocity, and inlet precursor concentration control the number of precursor molecules reaching the packed bed zone. High values for v_g , w_{pr} , or n_o increase the precursor excess number. Powder bed convection speed, bed height, powder bed surface area, and site area determine the rate of reactive sites available for ALD entering the precursor zone. To keep precursor excess near a desired value, some parameters can be adjusted on the fly (gas velocity, packed bed height, etc.) while others must be considered during the reactor design stage (i. e., precursor inlet width). Additional factors such as vibration amplitude (Fig. 9) and bed permeability influence the position of the reaction front but not the molar balance between flow rates.

The changing position of the reaction front has a complex relationship with the outlet gas composition (Fig. 12). Product gas analysis via mass spectrometry is the most common in-situ diagnostic available in particle ALD systems [22,29] and provides insight into reaction behavior through changes in the transient outlet gas composition data, but extrapolation of these trends to surface reaction behavior is not always straightforward. Product gas concentrations are continuously diluted by purge gas as the products travel from the reaction site to the reactor outlet. The outlet stream can be divided into three regions: an initial low-signal or "dead time" segment (t < 2.5s in Fig. 12b) when product gases have not had enough time to evolve and propagate to the outlet; a rising-signal region (2.5s < t < 7.5s in Fig. 12b) as precursor gas reaches the powder bed, reacts with many available surface sites, and spreads towards the packed bed inlet and outlet; and a moderate-signal region as the outlet gas composition equilibrates and only sites along the reaction front near the packed bed inlet are continuously producing product gas. An advancing reaction front can be accompanied by an increase in the outlet mole fraction of methane during the rising-signal phase (Fig. 12a and b) if the molar flow balance or reaction front size is also changing. High inlet mass fractions of precursor (i.e., $Y_{TMA} = 0.01$) spread and react quickly to produce a larger spike of methane in the rising signal region compared to slowly-propagating, low inlet mass

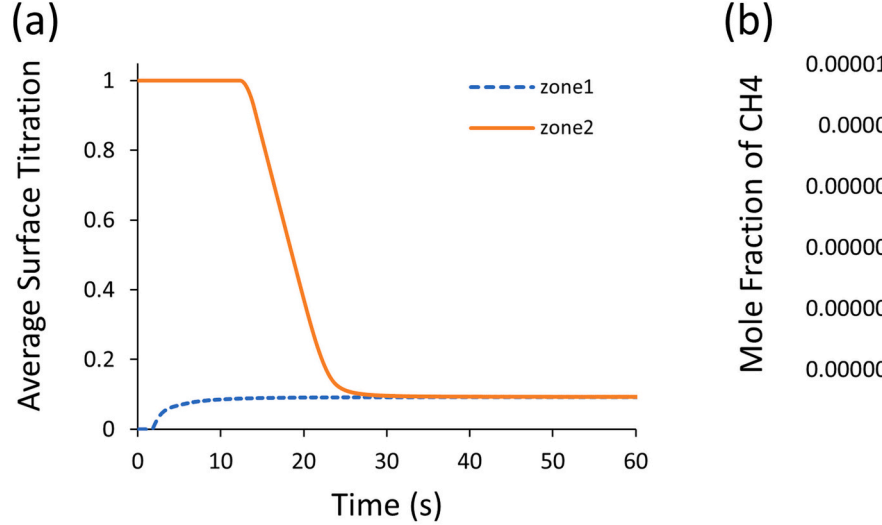
fractions of precursor.

3.3. Multiphase flow behavior during CVR-ALD, single ALD cycle

Single precursor zone models ignore the potential for CVD reactions caused by mixing between precursor zones. High excess numbers indicate unreacted precursor gas is leaving the packed bed zone and can be transported upwards to the reactor outlet or outwards towards the neighboring precursor zones. CVD reactions are not self-limited and can occur wherever both precursors come into contact. Spatially resolved full ALD cycle simulations provide information on the location and severity of parasitic volume reactions.

The full ALD cycle simulations exhibit similarities to the single precursor zone simulations. Quasi-steady surface titration uniformity and outlet gas composition results are observed after an equilibration period (Fig. 13). The bed starts with fully hydroxylated surface sites, so the bed is fully titrated in zone 2 ($\overline{\theta}_{OH}=1$) and incoming water vapor has nothing to react with until methylated sites from the TMA zone are conveyed into the water zone after $t\approx 15s$. Both half-reactions are fast and the quasi-steady reaction fronts occur at similar locations relative to the precursor inlet (Fig. 14a), leading to similar average surface titrations after an equilibration period of around 30 s. Methane mole fractions in Fig. 13b exhibit the same three regions discussed in Fig. 12b. No overshoot is seen in the outlet methane mole fraction for zone 2 because reactions occur at the interface with incoming methylated sites only.

The lack of methylated sites for the water half-reaction results in spillover of water vapor to neighboring TMA zones and subsequent CVD reactions (Fig. 14b). The expanding precursor front during the risingsignal phase has methylated sites to react with towards the packed bed inlet but no reaction sites towards the packed bed outlet. Adjusting inlet mass fractions to give near-unity excess numbers and a stoichiometric TMA/water ratio decreases the average CVD reaction rate by two orders of magnitude but does not completely prevent CVD (Fig. 15a). A pulse delay can be implemented between the start of the TMA dose and the start of the water dose to minimize water vapor spillover. A pulse delay of 15 s was observed to eliminate the startup spike in average reaction rate for the stoichiometric case and minimize initial CVD reaction prevalence without preventing complete surface titration uniformity at the packed bed outlet (Fig. 15b). Excess numbers equal to each half-reaction stoichiometric ratio are needed to prevent CVD reactions entirely.



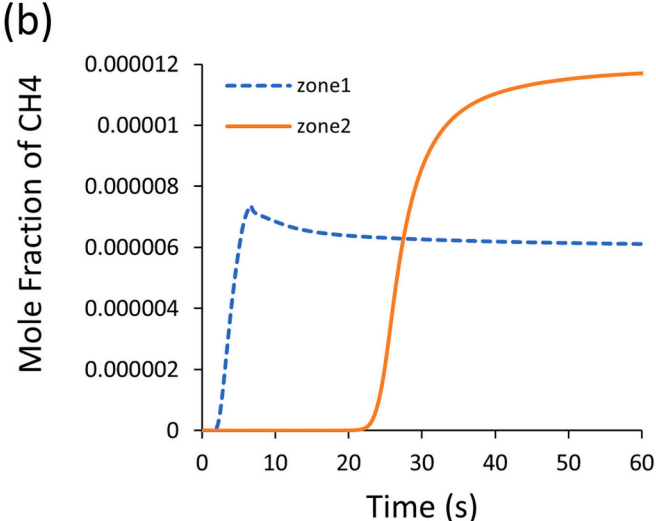


Fig. 13. Average surface titration over the blue boxed region from Fig. 10a (a) and mole fraction of methane (b) in the outlet gas streams for the first precursor zone and the second precursor zone when $Y_{TMA} = 0.0002$ and $Y_{H_2O} = 0.000075$. Surface titration refers to the sterically hindered coverage of $OAl(CH_3)_2$ for zone 1 or OH for zone 2 (For interpretation of the references to colour in this figure legend, the reader is referred to the web version of this article.)

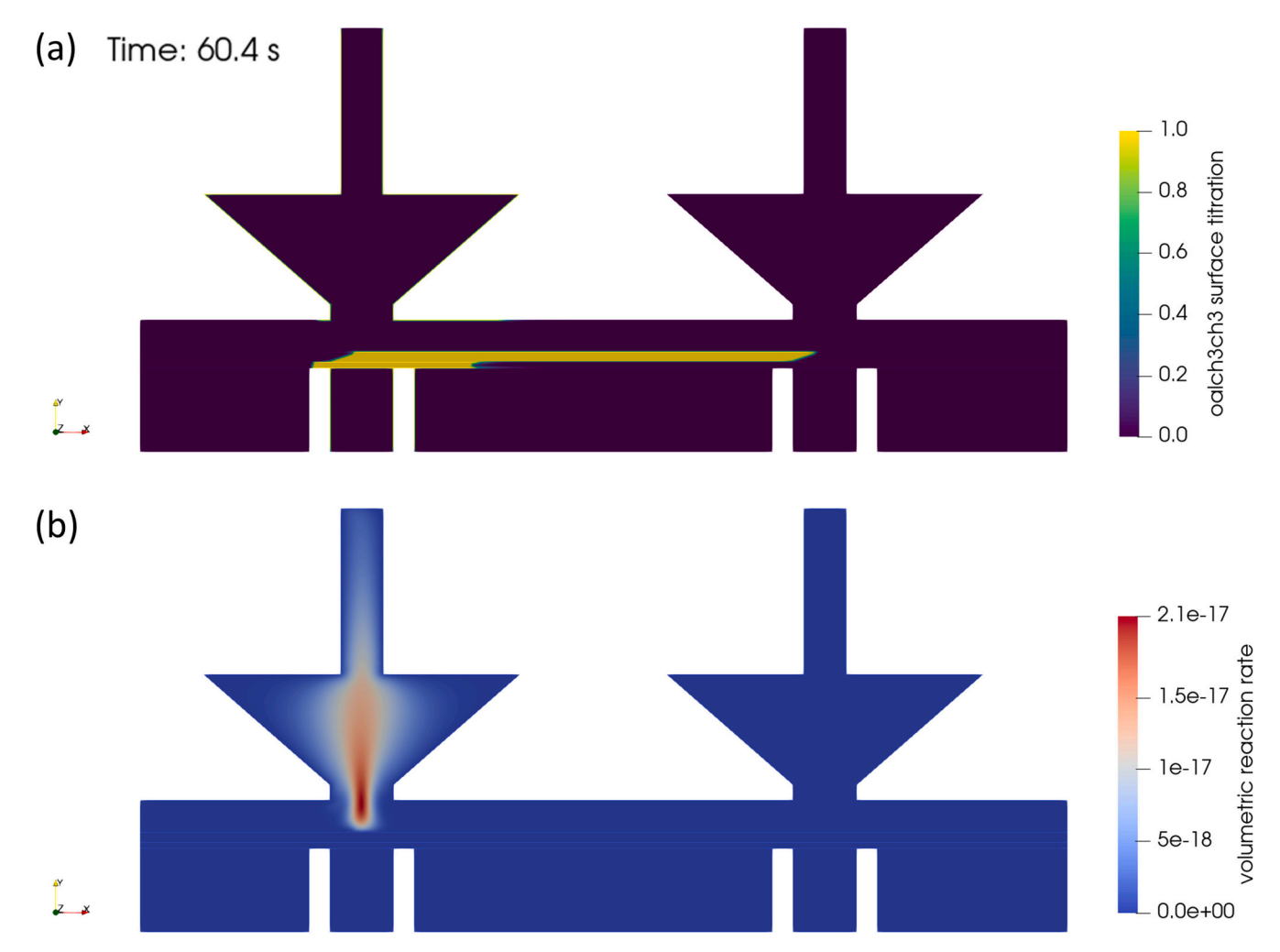


Fig. 14. Surface plots for surface titration of $OAl(CH_3)_2$ species (a) and CVD reaction rate in kgmol/m³-s (b) during a stoichiometric TMA/water dose ($Y_{TMA} = 0.0002, Y_{H_2O} = 0.000075$) at time t = 60.4 s

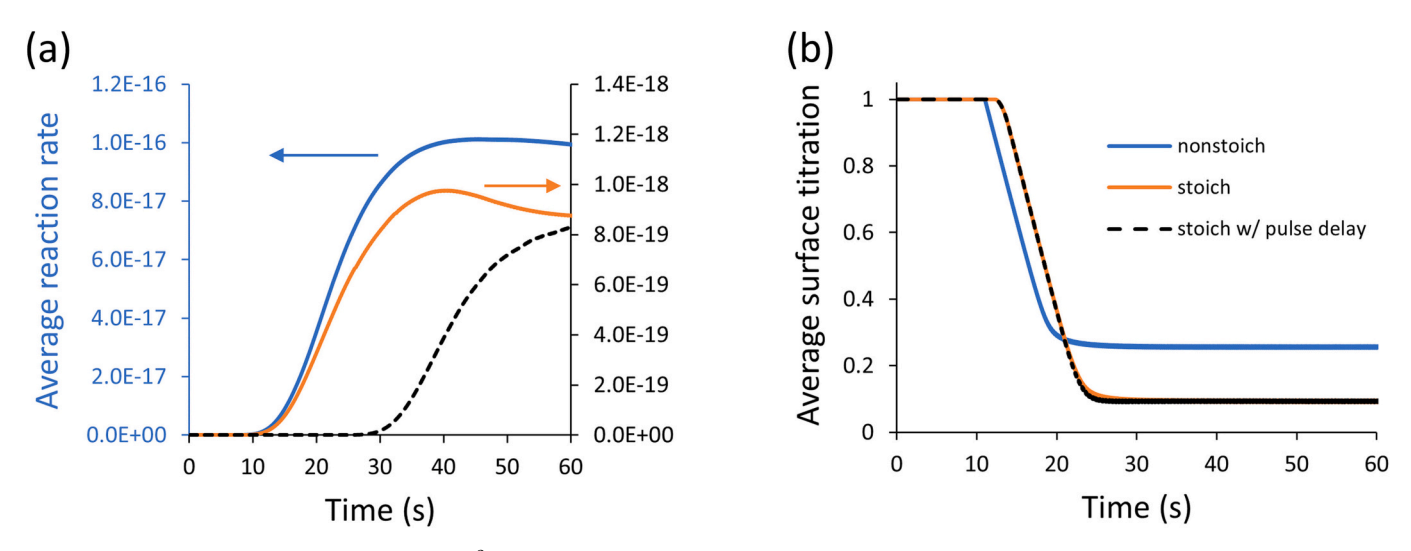


Fig. 15. Average volumetric reaction rate in kgmol/m³-s (a) and average surface titration of OH in zone 2 (b). Values are shown for a nonstoichiometric case ($Y_{TMA} = 0.001$ & $Y_{H_2O} = 0.001$), a stoichiometric case ($Y_{TMA} = 0.0002$ & $Y_{H_2O} = 0.000075$), and the same stoichiometric conditions with a 15-s pulse delay between the TMA and H₂O doses. In (a), the blue line reaction rate is labeled on the left vertical axis while the right vertical axis corresponds to the orange and black dashed lines (For interpretation of the references to colour in this figure legend, the reader is referred to the web version of this article.)

J. Hartig et al. Powder Technology 421 (2023) 118448

4. Conclusions

A moving porous media model capable of resolving reactor-scale flow behavior in CVR-ALD was presented. This study focused on multiphase flow behavior and operating conditions for TMA/water alumina ALD on $\geq\!20~\mu m$ diameter particle beds; future work will be needed to investigate more complex, temperature-dependent ALD kinetics [8,15,67] and finer substrate materials [29]. Empirically derived parameters such as sticking probability and surface site density can vary by orders of magnitude [78] from the values used in this study when working with slower chemistries. Key findings are included in the summary below.

All three porous media samples were advertised as 10-µm stainless-steel porous materials but differed significantly in mean through-pore size, tortuosity, porosity, and permeability. The mesh material has many large, open pore spaces that do not dictate primary flow channels based on MIP/CFP results and visual observations from the XRCT data. The felt and powder materials had tighter MIP pore size distributions with fewer large, open pores than the mesh material. Geometric anisotropies did not always correlate to strong anisotropy in the flow properties. As an example, the felt material has a clear 2D layered structure, but the through-thickness tortuosity (1.40) did not differ markedly from the in-plane tortuosities (1.63 and 1.72) based on the TauFactor simulation results.

In the range of attainable operating conditions for our CVR-ALD setup, some parameters were observed to modify bed surface titration and outlet gas streams more than others. Reactor vibration produced large fluctuations in the transient gas flow streamlines. Vibration had a diffusive effect on precursor concentration that increased with vibration magnitudes between $\Gamma=0.30$ and $\Gamma=0.60$. An increase in powder bed convection speed skewed the precursor concentration gradient towards the powder bed outlet. The reaction front advanced towards the powder bed inlet with higher inlet precursor mass fractions. Qualitative trends in the time evolution of surface titration and outlet product gas mole fraction were similar for all cases studied.

Concurrent dosing of TMA and water in the single ALD cycle simulations led to CVD reactions in the TMA zone. Stoichiometric ratios between the inlet TMA and water dose mole fractions and excess numbers near each half reaction stoichiometry are needed to minimize CVD prevalence. A balance must be struck between optimizing precursor utilization or CVD mitigation (low excess number) and guaranteeing surface titration uniformity (high excess number). Experimentally, water doses exceeding the stoichiometric ratio are often used to compensate for water adsorption on the reactor and tubing walls [79] so comparison to experiments would be necessary to determine the optimal excess number for each half-reaction.

The continuous spatial particle ALD simulation results share qualitative similarities to other continuum-scale studies on spatial ALD [13,14]. Purge gas zones are understood to minimize mixing between precursor gas zones, provided zone sizing and operating conditions are appropriate [9,14]. Precursor and byproduct gas signals at the outlet are observed to increase during reactor startup until reaching a quasi-steady state at the conditions explored in the simulations [13,14]. Similar trends are also observed in the fractional coverage or average surface titration with time [10,14]. Studies on moving substrates in other spatial ALD systems have also observed the precursor "dragging" effect caused by relative motion between the reactor and the substrate [9]. Comparing the excess number for a continuous spatial system (eq. 17) to a batch ALD system, a new dependence on dosing gas velocity v_g and packed bed convection speed \overline{u}_{pb} is introduced [77]. This study extends many continuum-scale observations from batch ALD and other spatial ALD systems to a continuous spatial particle ALD reactor configuration.

CRediT authorship contribution statement

Julia Hartig: Conceptualization, Data curation, Formal analysis,

Investigation, Methodology, Project administration, Software, Validation, Visualization, Writing – original draft, Writing – review & editing. Vidumin Dahanayake: Data curation, Formal analysis, Investigation, Resources, Visualization, Writing – review & editing. Julie Nguyen: Formal analysis, Methodology, Investigation, Resources. Carter Wilson: Formal analysis, Investigation, Resources. Austin M. Barnes: Investigation, Methodology, Resources. Alan W. Weimer: Funding acquisition, Project administration, Supervision, Writing – review & editing.

Declaration of Competing Interest

The authors declare the following financial interests/personal relationships which may be considered as potential competing interests:

A.W. Weimer has a significant financial interest in Forge Nano.

Data availability

Data will be made available on request.

Acknowledgements

Financial support from the National Science Foundation [NSF GOALI #1852824] is gratefully acknowledged. This work was also supported, in part, by the U.S. National Science Foundation (Award No. CBET-1726864). Analyses were performed at the MIMIC center at CU Boulder (RRID:SCR 019307).

References

- M. Shahmohammadi, R. Mukherjee, C. Sukotjo, U.M. Diwekar, C.G. Takoudis, Recent advances in theoretical development of thermal atomic layer deposition: a review, Nanomaterials 12 (2022) 831.
- [2] R.L. Puurunen, Random deposition as a growth mode in atomic layer deposition, Chem. Vap. Depos. 10 (2004) 159–170.
- [3] A. Yanguas-Gil, J.W. Elam, A Markov chain approach to simulate atomic layer deposition chemistry and transport inside nanostructured substrates, Theor. Chem. Accounts 133 (2014) 1–13.
- [4] J. Elam, D. Routkevitch, P. Mardilovich, S. George, Conformal coating on ultrahigh-aspect-ratio nanopores of anodic alumina by atomic layer deposition, Chem. Mater. 15 (2003) 3507–3517.
- [5] N. Cheimarios, D. To, G. Kokkoris, G. Memos, A.G. Boudouvis, Monte Carlo and kinetic Monte Carlo models for deposition processes: a review of recent works, Front. Phys. 9 (2021), 631918, https://doi.org/10.3389/fphy.
- [6] A. Lankhorst, B. Paarhuis, H. Terhorst, P. Simons, C. Kleijn, Transient ALD simulations for a multi-wafer reactor with trenched wafers, Surf. Coat. Technol. 201 (2007) 8842–8848.
- [7] M. Ylilammi, O.M. Ylivaara, R.L. Puurunen, Modeling growth kinetics of thin films made by atomic layer deposition in lateral high-aspect-ratio structures, J. Appl. Phys. 123 (2018), 205301.
- [8] A. Yanguas-Gil, J.A. Libera, J.W. Elam, Reactor scale simulations of ALD and ALE: ideal and non-ideal self-limited processes in a cylindrical and a 300 mm wafer cross-flow reactor, J. Vac. Sci. Technol. A 39 (2021), 062404.
- [9] W. Cong, Z. Li, K. Cao, G. Feng, R. Chen, Transient analysis and process optimization of the spatial atomic layer deposition using the dynamic mesh method, Chem. Eng. Sci. 217 (2020), 115513.
- [10] Y. Zhang, Y. Ding, P.D. Christofides, Multiscale computational fluid dynamics modeling of thermal atomic layer deposition with application to chamber design, Chem. Eng. Res. Des. 147 (2019) 529–544.
- [11] Z. Deng, W. He, C. Duan, B. Shan, R. Chen, Atomic layer deposition process optimization by computational fluid dynamics, Vacuum 123 (2016) 103–110.
- [12] G. Gakis, H. Vergnes, E. Scheid, C. Vahlas, B. Caussat, A.G. Boudouvis, Computational fluid dynamics simulation of the ALD of alumina from TMA and H2O in a commercial reactor, Chem. Eng. Res. Des. 132 (2018) 795–811.
- [13] D. Pan, T.-C. Jen, C. Yuan, Effects of gap size, temperature and pumping pressure on the fluid dynamics and chemical kinetics of in-line spatial atomic layer deposition of Al2O3, Int. J. Heat Mass Transf. 96 (2016) 189–198.
- [14] D. Pan, Numerical study on the effectiveness of precursor isolation using N2 as gas barrier in spatial atomic layer deposition, Int. J. Heat Mass Transf. 144 (2019), 118642.
- [15] M.R. Shaeri, T.-C. Jen, C.Y. Yuan, Reactor scale simulation of an atomic layer deposition process, Chem. Eng. Res. Des. 94 (2015) 584–593.
- [16] V. Cremers, R.L. Puurunen, J. Dendooven, Conformality in atomic layer deposition: current status overview of analysis and modelling, Appl. Phys. Rev. 6 (2019), 021302.
- [17] R.G. Gordon, D. Hausmann, E. Kim, J. Shepard, A kinetic model for step coverage by atomic layer deposition in narrow holes or trenches, Chem. Vap. Depos. 9 (2003) 73–78.

- [18] V. Dwivedi, R.A. Adomaitis, Multiscale simulation and optimization of an atomic layer deposition process in a nanoporous material, ECS Trans. 25 (2009) 115.
- [19] P.S. Maydannik, T.O. Kaariainen, D.C. Cameron, Continuous atomic layer deposition: explanation for anomalous growth rate effects, J. Vac. Sci. Technol. A 30 (2012) 01A122.
- [20] A. Yanguas-Gil, J.W. Elam, Analytic expressions for atomic layer deposition: coverage, throughput, and materials utilization in cross-flow, particle coating, and spatial atomic layer deposition, J. Vac. Sci. Technol. A 32 (2014), 031504.
- [21] V.E. Strempel, R. Naumann d'Alnoncourt, M. Drieß, F. Rosowski, Atomic layer deposition on porous powders with in situ gravimetric monitoring in a modular fixed bed reactor setup, Rev. Sci. Instrum. 88 (2017), 074102.
- [22] D.M. King, J.A. Spencer II, X. Liang, L.F. Hakim, A.W. Weimer, Atomic layer deposition on particles using a fluidized bed reactor with in situ mass spectrometry, Surf. Coat. Technol. 201 (2007) 9163–9171.
- [23] J. McCormick, B. Cloutier, A. Weimer, S. George, Rotary reactor for atomic layer deposition on large quantities of nanoparticles, J. Vac. Sci. Technol. A 25 (2007) 67-74
- [24] C.-L. Duan, X. Liu, B. Shan, R. Chen, Fluidized bed coupled rotary reactor for nanoparticles coating via atomic layer deposition, Rev. Sci. Instrum. 86 (2015), 075-101
- [25] J.R. van Ommen, D. Kooijman, M.D. Niet, M. Talebi, A. Goulas, Continuous production of nanostructured particles using spatial atomic layer deposition, J. Vac. Sci. Technol. A 33 (2015), 021513.
- [26] J. Hartig, H.C. Howard, T.J. Stelmach, A.W. Weimer, DEM modeling of fine powder convection in a continuous vibrating bed reactor, Powder Technol 386 (2021) 200, 222
- [27] D. Longrie, D. Deduytsche, C. Detavernier, Reactor concepts for atomic layer deposition on agitated particles: a review, J. Vac. Sci. Technol. A 32 (2014), 010802
- [28] I.J.A. Spencer, R.A. Hall, Continuous spatial atomic layer deposition process and apparatus for applying films on particles, Google Patents (2018).
- [29] A.W. Weimer, Particle atomic layer deposition, J. Nanopart. Res. 21 (2019) 9.
- [30] F. Grillo, M.T. Kreutzer, J.R. van Ommen, Modeling the precursor utilization in atomic layer deposition on nanostructured materials in fluidized bed reactors, Chem. Eng. J. 268 (2015) 384–398.
- [31] S.M. George, Atomic layer deposition: an overview, Chem. Rev. 110 (2010)
- [32] R.L. Puurunen, Growth per cycle in atomic layer deposition: a theoretical model, Chem. Vap. Depos. 9 (2003) 249–257.
- [33] E.H. Kennard, Kinetic Theory of Gases, McGraw-hill New York, 1938.
- [34] M.A. van der Hoef, M. van Sint Annaland, N. Deen, J. Kuipers, Numerical simulation of dense gas-solid fluidized beds: a multiscale modeling strategy, Annu. Rev. Fluid Mech. 40 (2008) 47–70.
- [35] J. Wang, Continuum theory for dense gas-solid flow: a state-of-the-art review, Chem. Eng. Sci. 215 (2020), 115428.
- [36] J. Jänchen, T.H. Herzog, K. Gleichmann, B. Unger, A. Brandt, G. Fischer, H. Richter, Performance of an open thermal adsorption storage system with Linde type a zeolites: beads versus honeycombs, Microporous Mesoporous Mater. 207 (2015) 179–184.
- [37] H. Choi, A. Mills, Heat and mass transfer in metal hydride beds for heat pump applications, Int. J. Heat Mass Transf. 33 (1990) 1281–1288.
- [38] B.A. Meyer, D.W. Smith, Flow through porous media: comparison of consolidated and unconsolidated materials, Ind. Eng. Chem. Fundam. 24 (1985) 360–368.
- [39] Ansys, Fluent 17.0 Theory Guide, ANSYS inc, 2015.
- [40] D. Beard, P. Weyl, Influence of texture on porosity and permeability of unconsolidated sand, AAPG Bull. 57 (1973) 349–369.
- [41] P.C. Carman, Fluid flow through granular beds, Trans. Inst. Chem. Eng. 15 (1937) 150–166.
- [42] A.W. Heijs, C.P. Lowe, Numerical evaluation of the permeability and the Kozeny constant for two types of porous media, Phys. Rev. E 51 (1995) 4346.
- [43] P. Xu, B. Yu, Developing a new form of permeability and Kozeny–Carman constant for homogeneous porous media by means of fractal geometry, Adv. Water Resour. 31 (2008) 74–81.
- [44] C.F. Berg, Permeability description by characteristic length, tortuosity, constriction and porosity, Transp. Porous Media 103 (2014) 381–400.
- [45] J. Bear, Dynamics of Fluids in Porous Media, Courier Corporation, 2013.
- [46] N. Epstein, On tortuosity and the tortuosity factor in flow and diffusion through porous media, Chem. Eng. Sci. 44 (1989) 777–779.
- [47] B. Lu, S. Torquato, Lineal-path function for random heterogeneous materials, Phys. Rev. A 45 (1992) 922.
- [48] M. Kaviany, Principles of Heat Transfer in Porous Media, Springer Science & Business Media, 2012.
- [49] A.A. Garrouch, L. Ali, F. Qasem, Using diffusion and electrical measurements to assess tortuosity of porous media, Ind. Eng. Chem. Res. 40 (2001) 4363–4369.

- [50] S.J. Cooper, A. Bertei, P.R. Shearing, J. Kilner, N.P. Brandon, TauFactor: an open-source application for calculating tortuosity factors from tomographic data, SoftwareX 5 (2016) 203–210.
- [51] S. Carniglia, Construction of the tortuosity factor from porosimetry, J. Catal. 102 (1986) 401–418.
- [52] L. Shen, Z. Chen, Critical review of the impact of tortuosity on diffusion, Chem. Eng. Sci. 62 (2007) 3748–3755.
- [53] R. Zhong, M. Xu, R.V. Netto, K. Wille, Influence of pore tortuosity on hydraulic conductivity of pervious concrete: characterization and modeling, Constr. Build. Mater. 125 (2016) 1158–1168.
- [54] S.J. Cooper, M. Kishimoto, F. Tariq, R.S. Bradley, A.J. Marquis, N.P. Brandon, J. A. Kilner, P.R. Shearing, Microstructural analysis of an LSCF cathode using in situ tomography and simulation, ECS Trans. 57 (2013) 2671.
- [55] F.A. Dullien, Porous Media: Fluid Transport and Pore Structure, Academic press,
- [56] B. Tjaden, S.J. Cooper, D.J. Brett, D. Kramer, P.R. Shearing, On the origin and application of the Bruggeman correlation for analysing transport phenomena in electrochemical systems, Curr. Opin. Chem. Eng. 12 (2016) 44–51.
- [57] J. Hartig, A. Shetty, D.R. Conklin, A.W. Weimer, Aeration and cohesive effects on flowability in a vibrating powder conveyor, Powder Technol. 408 (2022), 117724.
- [58] C.Q. LaMarche, S. Leadley, P. Liu, K.M. Kellogg, C.M. Hrenya, Method of quantifying surface roughness for accurate adhesive force predictions, Chem. Eng. Sci. 158 (2017) 140–153.
- [59] J. Katainen, M. Paajanen, E. Ahtola, V. Pore, J. Lahtinen, Adhesion as an interplay between particle size and surface roughness, J. Colloid Interface Sci. 304 (2006) 524-529
- [60] Y.I. Rabinovich, J.J. Adler, A. Ata, R.K. Singh, B.M. Moudgil, Adhesion between nanoscale rough surfaces: I. role of asperity geometry, J. Colloid Interface Sci. 232 (2000) 10–16.
- [61] M. Tahmasebpoor, L. de Martín, M. Talebi, N. Mostoufi, J.R. van Ommen, The role of the hydrogen bond in dense nanoparticle–gas suspensions, Phys. Chem. Chem. Phys. 15 (2013) 5788–5793.
- [62] K. Smith, J. Butterbaugh, S. Beaudoin, Effects of coating thickness on particle adhesion in microelectronics-based systems, ECS J. Solid State Sci. Technol. 2 (2013) P488.
- [63] ANSYS, #2002733 how Are Sticking Coefficient Reactions Converted into Arrhenius Rate Format? Solutions. Knowledge Resources. 2016.
- [64] H. Terao, H. Sunakawa, Effects of oxygen and water vapour introduction during MOCVD growth of GaAlAs, J. Cryst. Growth 68 (1984) 157–162.
- [65] N.I.o. Standards, Technology, NIST Chemistry WebBook, SRD 69, 2022.
- [66] C. Guerra-Nuñez, M. Döbeli, J. Michler, I. Utke, Reaction and growth mechanisms in Al2O3 deposited via atomic layer deposition: elucidating the hydrogen source, Chem. Mater. 29 (2017) 8690–8703.
- [67] R.L. Puurunen, Surface chemistry of atomic layer deposition: a case study for the trimethylaluminum/water process, J. Appl. Phys. 97 (2005) 9.
- [68] N. Hagihara, M. Kumada, R. Okawara, Handbook of Organometallic Compounds, 1968.
- [69] M.M. Tomadakis, T.J. Robertson, Viscous permeability of random fiber structures: comparison of electrical and diffusional estimates with experimental and analytical results, J. Compos. Mater. 39 (2005) 163–188.
- [70] V.D. Bruggeman, Berechnung verschiedener physikalischer Konstanten von heterogenen Substanzen. I. Dielektrizitätskonstanten und Leitfähigkeiten der Mischkörper aus isotropen Substanzen, Ann. Phys. 416 (1935) 636–664.
- [71] M.S. El-Sayed, Study of Transport Phenomena in Sandstone Samples in Relation to the Pore Structure, University of Waterloo (Canada), Ann Arbor, 1979, p. 1.
- [72] A. Koponen, M. Kataja, J. Timonen, Permeability and effective porosity of porous media, Phys. Rev. E 56 (1997) 3319.
- [73] R. Jones, H. Pollock, D. Geldart, A. Verlinden, Inter-particle forces in cohesive powders studied by AFM: effects of relative humidity, particle size and wall adhesion, Powder Technol. 132 (2003) 196–210.
- [74] M. Ciavarella, J. Joe, A. Papangelo, J. Barber, The role of adhesion in contact mechanics, J. R. Soc. Interface 16 (2019) 20180738.
- [75] A. Redford, G. Boothroyd, Vibratory feeding, in: Proceedings of the Institution of Mechanical Engineers 182, 1967, pp. 135–152.
- [76] A. Yanguas-Gil, J.W. Elam, Self-limited reaction-diffusion in nanostructured substrates: surface coverage dynamics and analytic approximations to ALD saturation times, Chem. Vap. Depos. 18 (2012) 46–52.
- [77] A. Yanguas-Gil, J.W. Elam, Diffusion-reaction model of ALD in nanostructured substrates: analytic approximations to dose times as a function of the surface reaction probability, ECS Trans. 41 (2011) 169.
- [78] J. Ferguson, K. Buechler, A. Weimer, S. George, SnO2 atomic layer deposition on ZrO2 and Al nanoparticles: pathway to enhanced thermite materials, Powder Technol. 156 (2005) 154–163.
- [79] A. Paranjpe, S. Gopinath, T. Omstead, R. Bubber, Atomic layer deposition of AlO x for thin film head gap applications, J. Electrochem. Soc. 148 (2001) G465.